RESEARCH ARTICLE

Metrological characterization of porosity graded β-Ti21S triply periodic minimal surface cellular structure manufactured by laser powder bed fusion

Lorena Emanuelli[1]*, Raffaele De Biasi[2], Anton du Plessis[3,4], Carlo Lora[5], Alireza Jam[2], Matteo Benedetti[2], Massimo Pellizzari[2]

[1]INSTM (Operative center: University of Trento), Trento, 38123, Italy

[2]Department of Industrial Engineering, University of Trento, Trento, Italy

[3]Research Group 3D Innovation, Stellenbosch University, Stellenbosch, South Africa

[4]Object Research Systems, Montreal, Canada

[5]SISMA SpA, Piovene Rocchette, Vicenza, Italy

(This article belongs to the *Special Issue: 3D Printing of Advanced Biomedical Devices*)

*Corresponding author: Lorena Emanuelli (lorena.emanuelli@unitn.it)

Abstract

The design of a functionally graded porous structure (FGPS) for use in prosthetic devices is crucial for meeting both mechanical and biological requirements. One of the most commonly used cellular structures in FGPS is the triply periodic minimal surface (TPMS) structure due to its ability to be defined by implicit equations, which allows for smooth transitions between layers. This study evaluates the feasibility of using a novel β-Ti21S alloy to fabricate TPMS-based FGPS. This beta titanium alloy exhibits low elastic modulus (53 GPa) and good mechanical properties in as-built condition. Two TPMS FGPSs with relative density gradients of 0.17, 0.34, 0.50, 0.66, and 0.83 and unit cell sizes of 2.5 mm and 4 mm were designed and fabricated using laser powder bed fusion (LPBF). The as-manufactured structures were analyzed using scanning electron microscopy (SEM) and X-ray micro-computed tomography (μ-CT), and the results were compared to the design. The analysis revealed that the pore size and ligament thickness were undersized by less than 5%. Compression tests showed that the stabilized elastic modulus was 4.1 GPa for the TPMS with a 2.5 mm unit cell size and 10.7 GPa for the TPMS with a 4 mm unit cell size. A finite element simulation was performed to predict the specimen's elastic properties, and a lumped model based on lattice homogenized properties was proposed and its limitations were explored.

1. Introduction

The mechanical and osteogenic properties are of primary importance in the selection of a biomaterial and in the design of an implant. The main requirements for a biomaterial include biocompatibility, high corrosion and wear resistance, high osteogenic response,

and mechanical properties similar to human bone[1]. Among the various biomaterials, metallic ones offer an ideal combination of mechanical and biological properties, making them suitable for long-lasting implants. Commonly used metallic materials in the orthopedic and dental fields are 316L, Co-based alloys, tantalum alloys, and titanium alloys[2]. Thanks to the excellent combination of high specific strength, high corrosion resistance, enhanced biocompatibility, and elastic modulus (110–52 GPa), titanium alloys are particularly suitable biomaterials for implants. The most common titanium alloy used in the orthopedic field is the standardized Ti-6Al-4V extra-low interstitial (ELI)[3] thanks to its excellent mechanical properties and biocompatibility. However, the release of metal ions such as Al and V can lead to severe metabolic bone diseases and neurological disorders[4-6]. Additionally, V ions are cytotoxic[4]. Furthermore, to achieve the desired mechanical performances, a post-thermal treatment must typically be applied to transform martensite into a less brittle α + β microstructure. The presence of undesirable elements, the need for a further thermal treatment, and the very high elastic modulus of Ti-6Al-4V have led to the development of the second generation of titanium alloys, based on the β phase microstructure. These novel biomaterials result in a decreased elastic modulus and a reduction of the harmful elements with good strength and corrosion resistance already after the additive manufacturing (AM) production process[7,8]. Three wrought β titanium alloys are standardized, namely Ti-15Mo[9], Ti-12Mo-6Zr-2Fe[10], and Ti-15Mo-5Zr-3Al[11]. The body-centered cubic (bcc) structure of β phase permits to obtain a lower stiffness thanks to its low intrinsic elastic modulus with additional good mechanical properties and extraordinary corrosion resistance and biocompatibility. Unfortunately, β Ti-15Mo is characterized by a low strength compared to Ti-6Al-4V and a strong tendency to the brittle ω phase precipitation[12]. To achieve higher mechanical strength, the addition of other elements is necessary. The β Ti-12Mo-6Zr-2Fe alloy in the as-built condition shows higher mechanical strength compared to Ti-15Mo but also higher elastic modulus similar to Ti-6Al-4V due to unwanted α^{II} phase precipitation inside β microstructure[13,14]. A decrease in the elastic modulus is achieved by changing the scanning strategy and application of a postsolution heat treatment which permits a significant increase in the intensity of the {100}<001> texture leading to an elastic modulus of around 75 GPa[13]. For Ti-15Mo-5Zr-3Al, an elastic modulus of 80 GPa and a strength around 900 MPa, with the latter being close to the one of Ti-6Al-4V, can be achieved by the alloy[15]. Recent studies have highlighted the promising performances of a un-standardized metastable β alloy (β-Ti21S) with the chemical composition of Ti-15Mo-3Nb-3Al-0.2Si (wt.%)[16-18]. It displays a β phase microstructure with a textured

columnar structure oriented along the building direction. This alloy exhibits lower Young's modulus of 52 GPa with a variation of less than 20% due to the texture, A good mechanical strength of around 830 MPa, an extraordinary fracture elongation of 21%, and a lower cytotoxicity compared to Ti-6Al-4V[17].

The human bone is composed of the external dense cortical part and the internal porous, namely trabecular one [1]. The cortical bone confers high strength, while the trabecular bone promotes the vascularization and flow of nutrients for continued bone remodeling. The stiffness of bones varies depending on their location. Cortical bone has an elastic modulus ranging from 4 to 30 GPa, while trabecular bone has a modulus between 0.1 and 4 GPa. However, the elastic modulus of the Ti21S alloy is still higher compared to that of human bone, which can cause a stress shielding effect. This occurs when the higher stiffness of the implant material prevents the transfer of mechanical stress to the surrounding bone, resulting in bone resorption and implant loosening. To prevent this effect and promote bone tissue growth, a prosthetic device with both high strength and low modulus similar to bone is preferred. One solution to reduce the bulk stiffness of the implant is to create a porous structure that more closely matches the stiffness of the surrounding bone[19]. Design and optimization of cellular structures to merge optimal mechanical properties and osteointegration are a core issue of recent studies in the engineering biological field[1,19,20-25]. The production of complex and even smaller cell geometries is made possible thanks to AM processes, such as laser powder bed fusion (LPBF), selective laser sintering (SLS), and selective electron beam melting (SEBM), which is also known as electron beam powder bed fusion. Energy sources, such as laser in LPBF and SLS and electron beam in SEBM, are used to selectively melt or sinter layers of metal powders to form the cellular structure[26]. The optimization of the processing parameters namely power, scan speed, hatch spacing, layer powder thickness, and chamber environment are of fundamental importance to obtain a nearly defect-free component[27]. Otherwise, internal defects such as lack of fusion, keyhole porosity, and cracks can form. Manufacturing imperfections due to the printing process, namely variation of the cross-section, excess of material at the junction between struts or ligaments, and strut waviness, can modify the final mechanical response of the cellular structure[18,28,29]. The mechanical properties of a porous metal are also affected by the unit cell architecture and the ratio between the density of the structure and the density of the material, namely the relative density. During an external compression load, the cellular structures may undergo deformation as a result of stretching, bending, and twisting of the struts and ligaments. The elastic modulus E

and the yield strength σ_y of the cellular structures have been correlated to relative density using Gibson–Ashby model[19], according to Equations I and II.

$$\frac{E}{E_0} = C_1 \left(\frac{\rho}{\rho_0} \right)^{n_1} \tag{I}$$

$$\frac{\sigma}{\sigma_0} = C_2 \left(\frac{\rho}{\rho_0} \right)^{n_2} \tag{II}$$

where

  E = elastic modulus of the cellular structure

  E_0 = elastic modulus of the bulk alloy

  ρ = density of the cellular structure

  ρ_0 = density of the bulk alloy

C_1, C_2, n_1 and n_2 are the Gibson–Ashby constants. n_1 and n_2 result equal to 2 and 3/2 for bending dominated behavior and equal to 1 and 1 in case of stretching-dominated behavior, respectively. The cellular structures are divided into two main groups, the strut-based lattices and the triply periodic minimal surface (TPMS) structures[30]. A main difference is the presence of struts and nodes in the strut-based lattices, while the TPMS shows a smoother transition at the connection point of the ligaments. The sharp notches formed at the junction between struts act as local stress concentrations and are deleterious in terms of fatigue resistance. This does not occur in the TPMS structures, where no sharp notches are present since they are characterized by mean surface curvature at each point equal to zero[23,31-37]. Thanks to these features, they are characterized by a high compression fatigue resistance of around 60% of the yield stress in case of Ti-6Al-4V[38]. TPMS structures are divided into two subgroups that are skeletal or sheet TPMS-based structures depending on the way they are created, by thickening the minimal surface or by solidifying the volumes between the minimal surfaces, respectively[39]. Skeletal TPMS structures are characterized by an interconnected porosity and a lower elastic modulus with respect to the sheet TPMS[26,32-35,37,40]. Al-Ketan *et al.*[26] compared strut-based cellular structures, namely Kelvin and Octet-truss, with sheet and skeletal-TPMSs. They highlighted the lower elastic modulus of the skeletal-based structures. In detail, skeletal-based Schoen's I-graph-wrapped package (IWP) results in the one with the lowest quasi-elastic modulus. Nevertheless, lower values of the peak stress and the toughness are achieved in the skeletal-based TPMS. Comparing the diamond, IWP, and gyroid geometries, skeletal-based gyroid TPMS offers the right compromise between a low elastic modulus and a good strength. Since cancellous bone has a TPMS-like structure, application of TPMS structure in porous prosthetic devices

to optimize not only the mechanical performances but also the bone regeneration seem to be one of the most promising solutions[41]. By modifying the shape, the porosity and the pore size of TPMS structures, it is possible to achieve a structure with great surface curvature and permeability to promote bone regeneration[1,42].

Going inside a human bone, it is possible to observe a variable porosity of the trabecular structure depending on the position inside it[43]. Creating a graded porosity inside the structures, namely functionally graded porous structures (FGPSs), is of fundamental importance to attain mechanical and biological efficiency in terms of high strength, low stiffness, and improved tissue ingrowth. Indeed, a pore size in the range of 100–600 μm is essentially on the side where osseointegration must be guaranteed[26,44-46]. Higher density level is desired in the junction with the solid part or where wear resistance must be high. Differently, maximum porosity level is desired inside the implant to reduce even more the stiffness of the prosthetic device[37,40,47,48]. In the recent years, different authors have focused their attention on the design of cellular structure with a gradient porosity, both in the case of strut-based and TPMS structures[25,32,33,47,49-53]. The nature of TPMS unit cells to be defined by implicit equations and to be optimized to achieve optimal mechanical properties and promote bone ingrowth makes them a promising solution in the case of FGPSs. Indeed, they avoid the problem of discontinuity between layers that occurs with trabecular unit cells[32,33,47,53-55]. The effect of the FGPS on the mechanical response was evaluated by de Galarreta *et al.*[56] under a quasi-static compression load. They demonstrated a mixture rule dependency between the elastic modulus and the porosity level in the case of radially graded porous structure. A different behavior is exhibited by longitudinally graded structures, where the elastic modulus of the entire structure is dominated by the collapse of the weakest layer of the FGPSs. The correlations between the overall elastic modulus of the FGPS and the single value associated with the different porosity levels are shown in Equations III and IV in the case of longitudinal and radial/lateral porous graded structures, respectively[56].

$$\frac{1}{E} = \sum_{i=1}^{n} k_i \frac{1}{E_i} \tag{III}$$

$$E = \sum_{i=1}^{n} k_i E_i \tag{IV}$$

n refers to the total number of layers, k_i the volume fraction of the corresponding layer with respect to the total volume, E the elastic modulus of the FGPSs, and E_i the elastic modulus of the corresponding layer i.

To the best of our knowledge, manufacturability and mechanical properties of TPMS-FGPS structures made
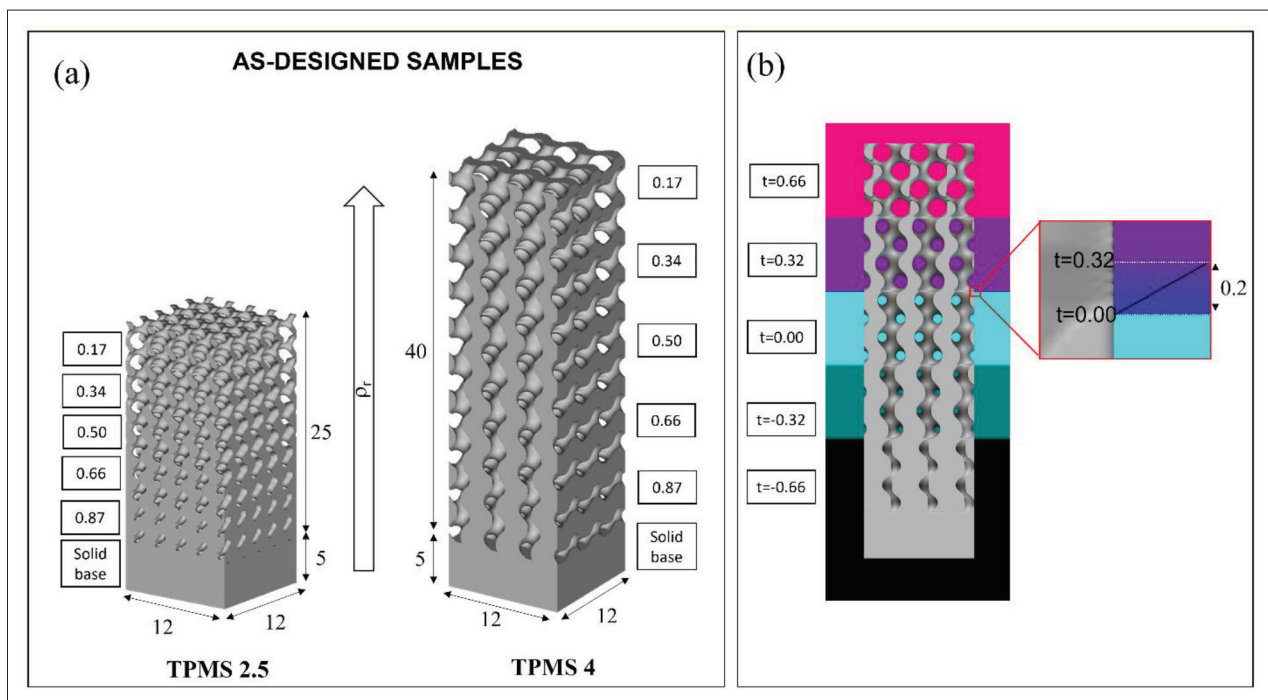
Figure 1. (a) Geometrical details of as-designed TPMS-FGPS 2.5 and 4.0 mm and (b) color mapping of the different level constant "t" values used to design the density levels and a detail of the linear ramp, having a length of 0.2 mm, generated between the level constants to connect the different porosity levels continuously.

by β-Ti21S titanium alloy have not been studied yet. To fill this gap, the present paper is aimed at investigating the manufacturability of skeletal-based gyroid TPMS structures in β-Ti21S alloy manufactured via LPBF with a porosity gradient. In detail, two skeletal-based gyroid TPMS cells with different sizes (2.5 and 4.0 mm) were investigated.

2. Materials and experimental procedures

2.1 Specimen design and preparation

Two different skeletal-based gyroid TPMS–FGPSs with unit cell size of 2.5 (TPMS-FGPS 2.5) and 4 mm (TPMS-FGPS 4) are designed by means of nTopology software, and the geometrical details are summarized in Figure 1a. Gyroid TPMS surface is defined by the implicit Equation V

$$G = \cos\cos\left(\frac{2\pi x}{L}\right)\sin\sin\left(\frac{2\pi y}{L}\right) + \cos\cos\left(\frac{2\pi y}{L}\right)\sin\sin\left(\frac{2\pi z}{L}\right)$$
$$+ \cos\cos\left(\frac{2\pi z}{L}\right)\sin\sin\left(\frac{2\pi x}{L}\right) - t = 0 \qquad (V)$$

where L is the cell size, and t is the level constant which defines the desired relative density of the structure. Both structures are characterized by 0.17, 0.34, 0.50, 0.66, and 0.83 relative density levels and a height of the levels of 2-unit cells. The level constants used to obtain the desired relative densities in both structures are summarized in Table 1.

Table 1. Level constants used to obtain all the different relative density levels in both TPMS-FGPSs

ρ_r CAD (–)	Level constant (t) TPMS 2.5 (–)	Level constant (t) TPMS 4 (–)
0.17	−0.41	−0.66
0.34	−0.20	−0.32
0.50	0.00	0.00
0.66	0.20	0.32
0.83	0.40	0.66

A linear ramp, having a length of 0.2 mm, is generated between the level constants to connect the different porosity levels continuously (Figure 1b). A square base of 12 × 12 mm is used for both TPMS-FGPSs corresponding to around 5 × 5 and 3 × 3 cells for TPMS-FGPS 2.5 and TPMS-FGPS 4, respectively. The height of the porous specimens depends on the unit cell size and is of 25 mm and 40 mm for TPMS-FGPS 2.5 and TPMS-FGPS 4, respectively. A solid base with a thickness of 5 mm is added at the bottom of the structure to evaluate the connection between porous and bulk parts. The highest relative density level is designed to improve osseointegration thanks to the smaller pore size, while the lowest density permits to decrease the elastic modulus close to that of the cancellous bone. All computer-aided design (CAD)

Table 2. Geometrical details of the as-designed TPMS-FGPSs.

L (mm)	ρ_r CAD (–)	Level constant (t) (–)	Ligament thickness CAD (mm) [a]	Pore size CAD (mm) [a]	Ligament thickness CAD_max (mm) [b]	Pore size CAD_max (mm) [b]
2.5	0.17	−0.41	0.72 ± 0.01	1.56 ± 0.18	0.73	1.74
	0.34	−0.20	1.00 ± 0.01	1.38 ± 0.06	1.01	1.44
	0.50	0.00	1.25 ± 0.01	1.15 ± 0.05	1.27	1.20
	0.66	0.20	1.48 ± 0.04	0.92 ± 0.03	1.52	0.95
	0.83	0.40	1.66 ± 0.16	0.64 ± 0.02	1.82	0.66
4.0	0.17	−0.66	1.39 ± 0.04	1.99 ± 0.39	1.43	2.38
	0.34	−0.32	1.63 ± 0.08	1.90 ± 0.22	1.71	2.12
	0.50	0.00	1.84 ± 0.12	1.74 ± 0.14	1.96	1.88
	0.66	0.32	2.04 ± 0.16	1.54 ± 0.10	2.20	1.64
	0.83	0.66	2.10 ± 0.37	1.30 ± 0.06	2.47	1.36

[a] Data expressed as median ± MAD
[b] Data expressed as median + MAD

parameters are characterized by means of 3D image analysis software (ORS-Dragonfly) and are summarized in Table 2. Ligament thickness and pore size are calculated by means of the wall thickness analysis method which permits to obtain the size distribution of the analyzed 3D elements. This method evaluates the local thickness of the ligament or pore, by fitting its volume with the maximum spheres at each location in the 3D structure[57,58]. In view of the non-normal distribution of the values and the measurement frequencies shown in Figure 2 (the values are reported only for TPMS-FGPS 2.5 because of similar results in the case of TPMS-FGPS 4), median and median absolute deviation (MAD), rather than mean and standard deviation, are used to define the pore size and ligament thickness. Nevertheless, considering the size distribution of both pores and ligaments shown (Figure 2), smaller values are present with a frequency lower than 5% and only the highest values are detected with frequency in the range of 5%–50%. Therefore, in the case of relative densities with high ligament thickness (ρ_r = 0.83, Figure 2a) and high pore size (ρ_r = 0.17, Figure 2b), the median value (black dashed line) is poorly representative of the largest population of the distribution. The median and MAD values reported in Table 2 highlight that the MAD values increase when the size of pore or ligament increases. Under these circumstances, the higher number of low values with a frequency inferior to 5% affects the median value of the distribution that becomes not representative of the real pore size and/or ligament thickness. To avoid this inconsistency and to obtain a more representative dimensional value for the pore size or ligament thickness for the different relative densities, sum of median and

MAD (red dashed line in Figure 2) is computed. For illustrative purposes, the ligament thickness distribution and color mapping associated with the measurement in case of higher relative density for TPMS 2.5 are shown in Figure 3. Median value equal to 1.66 (blue in the mapping figure) results in an underestimate of the thickness, since major parts of the ligaments are around 1.80 (orange-red parts). The sum of median and MAD of 1.82 results are closer to the real values. Since a reference dimension is essential for comparing the as-designed specimen with the as-manufactured one, sum of median and MAD, namely CAD_max in Table 2, of the pore size and ligament thickness of the different relative densities is used. Pore size of the TPMS-FGPS 4.0 designed to have same relative density levels of TPMS-FGPS 2.5, results in a lower pore size of 1.36 mm (lower relative density level of 0.17) too large for the osseointegration requirement where a pore size in the range of 100–600 µm is necessary to optimize bone regeneration[25,44-46]. Correlations between relative densities (ρ_r), ligament thickness (l_t), and pore size (p_s) with the level constant "t" are evidenced in Figure 4, and the corresponding third-degree polynomial fitting are summarized in Equations VI–VIII and IX–XI for TPMS-FGPS 2.5 and TPMS-FGPS 4.0, respectively[47].

$$\rho_{r2.5} = 0.500 + 0.799t + 7.080E^{-17}t^2 + 0.038t^3 \quad Adj\ R^2 = 1$$
$$(VI)$$

$$l_{t2.5} = 1.266 + 1.258t + 0.051t^2 + 0.424t^3 \quad Adj\ R^2 = 0.99981$$
$$(VII)$$

$$p_{s2.5} = 1.197 - 1.196t + 0.017t^2 - 0.719t^3 \quad Adj\ R^2 = 0.99987$$
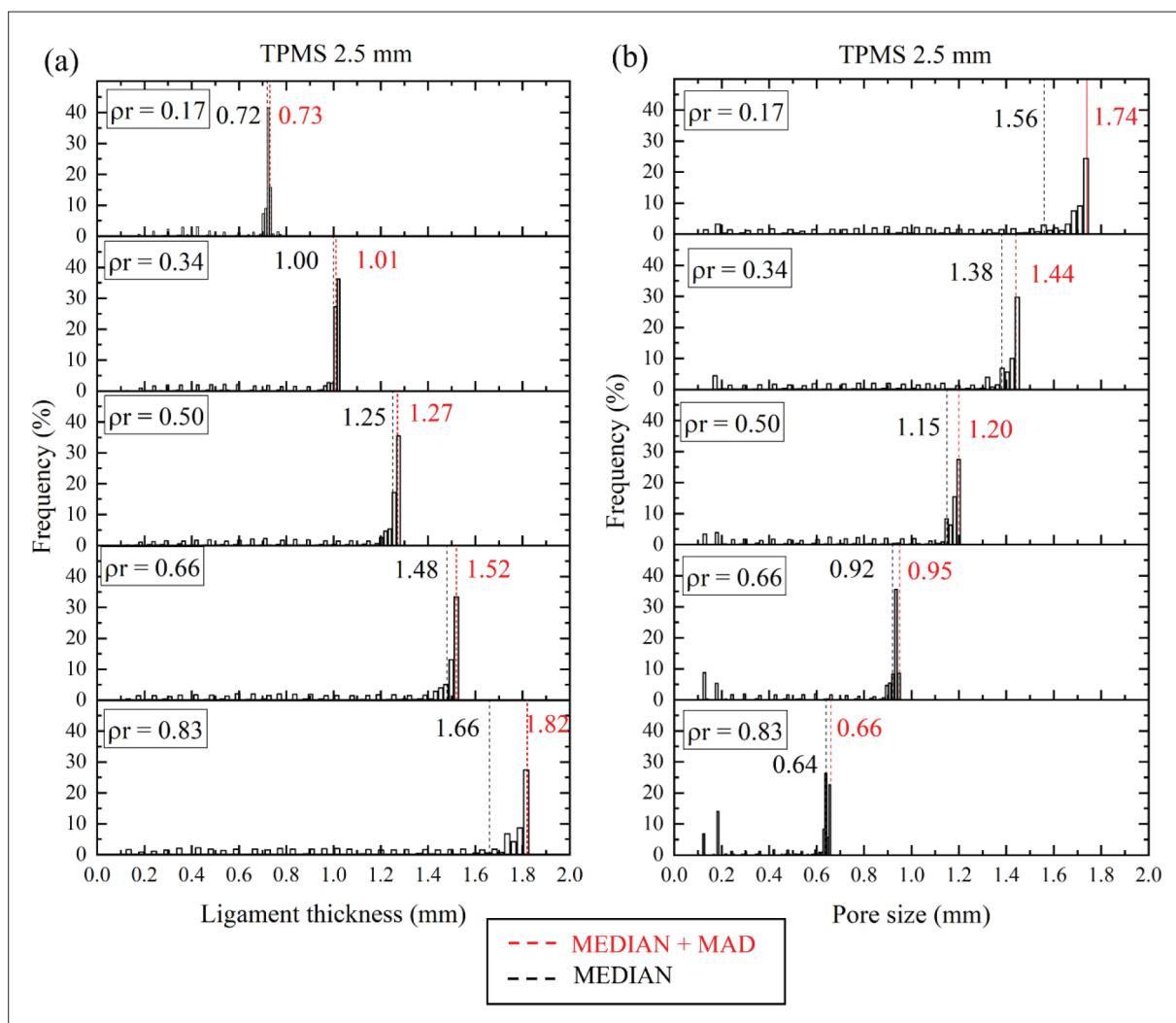$$(VIII)$$

Figure 2. Size distributions of all five relative density levels in case of (a) ligament thickness and (b) pore size for as-designed TPMS-FGPS 2.5. (red dashed line = median + MAD; black dashed line = median).

$$\rho_{r4.0} = 0.500 + 0.500t - 2.137E^{-16}t^2 + 6.541E^{-16}t^3 \quad Adj\ R^2 = 1 \tag{IX}$$

$$l_{t4.0} = 1.958 + 0.759t - 0.019t^2 + 0.067t^3 \quad Adj\ R^2 = 0.99996 \tag{X}$$

$$p_{s4.0} = 1.882 - 0.743t - 0.026t^2 - 0.068t^3 \quad Adj\ R^2 = 0.99997 \tag{XI}$$

Five samples for the two different FGPSs were printed by means of a LPBF machine model MYSINT100 (SISMA SPA, Piovene Rocchette, Italy) on a platform of 100 mm in Ar atmosphere, with a laser spot size of 55 μm, a power of 200 W and a volumetric energy density between 40 and 90 J/mm³ (Figure 5). A 45° alternate scan strategy was used. A prealloyed plasma atomized powder β-Ti21S alloy produced by GKN Hoeganaes Corporation (Cinnaminson, NJ, USA) was used. It was characterized by a powder size

distribution of 25–60 μm and the chemical composition as summarized in Table 3.

2.2. Metrological and material characterizations

2D (scanning electron microscopy [SEM] analysis) and 3D (micro-computed tomography [μ-CT] scan) metrological characterizations were used to characterize the as-manufactured samples. A JEOL IT 300 SEM apparatus equipped with EDX Bruker XFlash detector 630M with an active detector area of 30 mm² was used to acquire micrographs of 10 pores and 10 ligaments for each level of density. The corresponding mean and the standard deviation were calculated. μ-CT scan by means of the Nanotom S system with an X-ray voltage between 100 and 130 kV, a current of 80–90 μA, and a voxel size of 25 μm for each sample was used to perform the 3D metrological investigation. The wall thickness method, through the
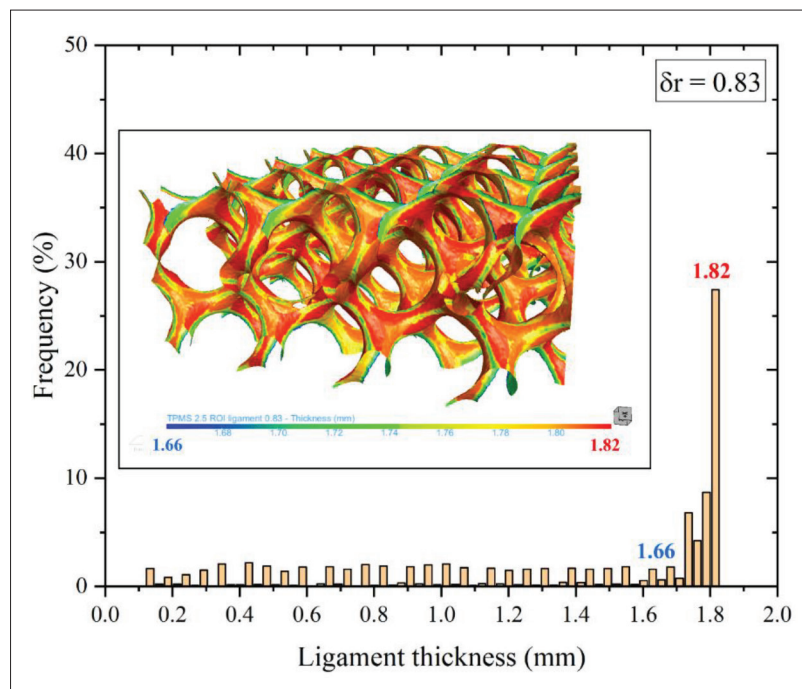
Figure 3. Example of wall thickness method results obtained in the case of TPMS 2.5 with a relative density of 0.83: visualization of the thickness measurement and ligament thickness distribution.
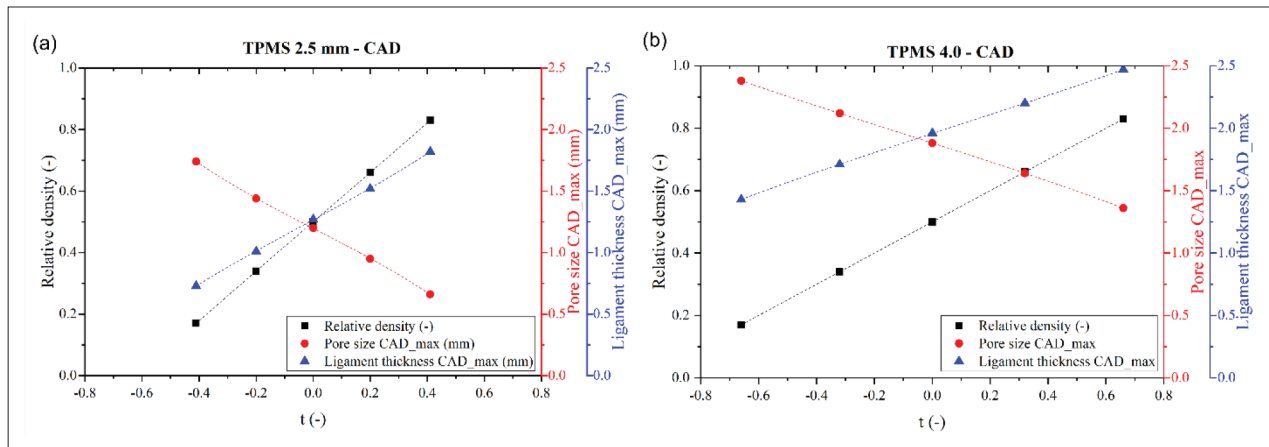

Figure 4. Correlations between relative density, ligament thickness and pore size with level constant "t" and corresponding equations obtained with a third-degree polynomial fitting in the case of (a) TPMS 2.5 and (b) TPMS 4.0.

ORS-Dragonfly software, was used to measure the ligament thickness and pore size distribution. As demonstrated by CAD metrological characterization, sum of median and MAD ligament and pore size was used to characterize the as-manufactured samples and to compare with the as-design specimens. In addition, overlapping of as-manufactured and of as-designed samples was performed, thanks to the align function and generation of a contour mesh in Dragonfly ORS software.

The microstructural characterization is carried out after standard metallographic preparation of the cross-

section. Kroll's reagent (1 mL of HF, 30 mL of HNO_3, 85 mL of distilled water) according to ASTM E407-07[59] was used to highlight the microstructure of the cross-section. Quasi-static compression tests were carried out by means of a servo-hydraulic Instron testing machine equipped with a linear variable differential transformer (LVDT) transducer to remove the machine compliance. The machine was operated under stroke control imparting a crosshead speed of 1 mm/min. Three specimens for each TPMS-FGPS geometry were tested at room temperature (20°C ± 3°C) according to ISO 13314:2011[60].
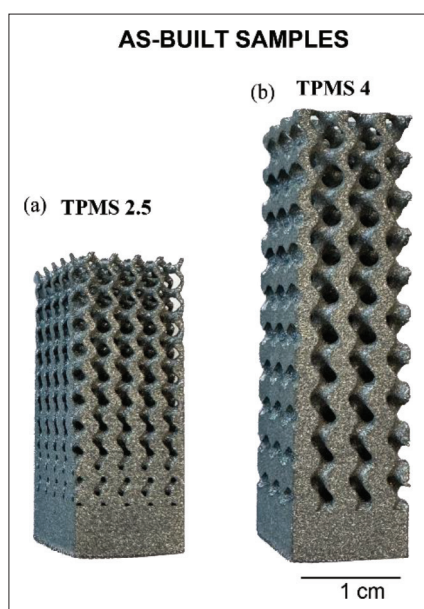
Figure 5. Details of the as-built TPMS-FGPS 2.5 and TPMS-FGPS 4.0.

Cyclic stabilized Young's modulus for each geometry was calculated by applying five loading-unloading compression ramps between 20% and 70% of the yield stress[61,62]. Numerical homogenization method, which replaces the single unit cell with an equivalent bulk elastic material model and with equivalent mechanical response of the lattice, was used to predict the elastic modulus of the different layers[63-66]. A convergence analysis was performed to define a suitable mesh size (0.05 mm) for the homogenization process. The mechanical properties of Ti-21S bulk material evaluated by Pellizzari *et al.*[17] were used. The homogenized mechanical properties were computed both on unit cell with as-designed (E_{nom}^{hom}) and as-manufactured (E_{real}^{hom}) ligament thickness, defined by wall thickness method, by referring to the associated level constant (t) of the TPMS geometry, at all different levels of relative density. The corresponding TPMS-FGPS elastic modulus values were calculated by Equation II and compared with the experimental data. Since high discrepancy between experimental and simulation values, in the case of TPMS-FGPS 4.0, a finite element analysis (FEA) of the complete specimen was performed. To confirm the result, the entire TPMS-FGPS 2.5 was simulated with FEA. The simulations were performed using the Workbench 2022 R2 (ANSYS, USA) software using solid element SOLID187. The contour mesh of the as-manufactured samples was obtained by means of Dragonfly ORS software and decimated using the nTopology 3.35.2 software (nTopology Inc., USA) to obtain the more realistic sample geometries. The mesh used for the FEA has a target dimension equal to

Table 3. The chemical composition of β-Ti21S (wt.%).

Element	Mo	Al	Nb	Si	O	Ni	Fe
Weight %	14.6	2.8	2.8	0.3	0.11	0.004	Bal.

0.3 mm, and its suitability was verified by performing a convergency analysis. The specimen loading condition resembled the experimental condition, i.e., a fixed constraint on the bottom surface of the specimen and a fixed displacement equal to 0.1 mm in the vertical direction on the top surface. The elastic modulus was computed with Equation XII.

$$E = \frac{F_z/A}{\Delta l/l_0} \qquad (XII)$$

where F_z is the reaction force on the bottom surface, A is the surface perpendicular to the applied load (around 12 × 12 mm), Δl is the fixed displacement equal to 0.1 and l_0 is the height of the FGPS samples (around 45 mm in case of TPMS-FGPS 4.0 and 30 mm in case of TPMS-FGPS 2.5).

3. Results and discussion

3.1. 2D and 3D metrological characterizations

2D metrological characterization using SEM analysis was carried out on the lateral surface of both TPMS-FGPSs to evaluate the ligament thickness and the pore size in the five relative densities. A SEM inspection of the top surface is possible only for the lower relative density (0.17). Figures 6 and 7 show micrograph details of the different relative density levels of TPMS-FGPS 2.5 and TPMS-FGPS 4, respectively. Comparing the lateral and the top view of 0.17 relative density, the orientation with respect to the building direction exerts a negligible influence on the ligament and pore size. No discontinuities between the different layers were detected in both TPMS-FGPSs, making these structures a promising solution in the case of FGPSs. The ligament thickness and pore size of the different relative density levels for both TPMS structures are summarized in Table 4 and compared with the CAD values. The percentage deviations with respect to CAD highlight an undersizing effect on both ligament and pore (Figure 8). For the ligament size, a maximum variation of 16% (TPMS-FGPS 2.5) and 9% (TPMS-FGPS 4.0) was observed, while for the pore size, it raised to 66% (TPMS-FGPS 2.5) and 64% (TPMS-FGPS 4.0), respectively. Figure 9 highlights the surface irregularities, roughness, and unmelted powders on the ligament surfaces in both TPMS-FGPSs. The excess of material and higher amount of unmelted powder in the upper part of the pores (Figure 9c) with respect to the lower one (Figure 9d) explain the undersizing of the pore with respect to CAD nominal dimensions. The high deviations in terms of pore
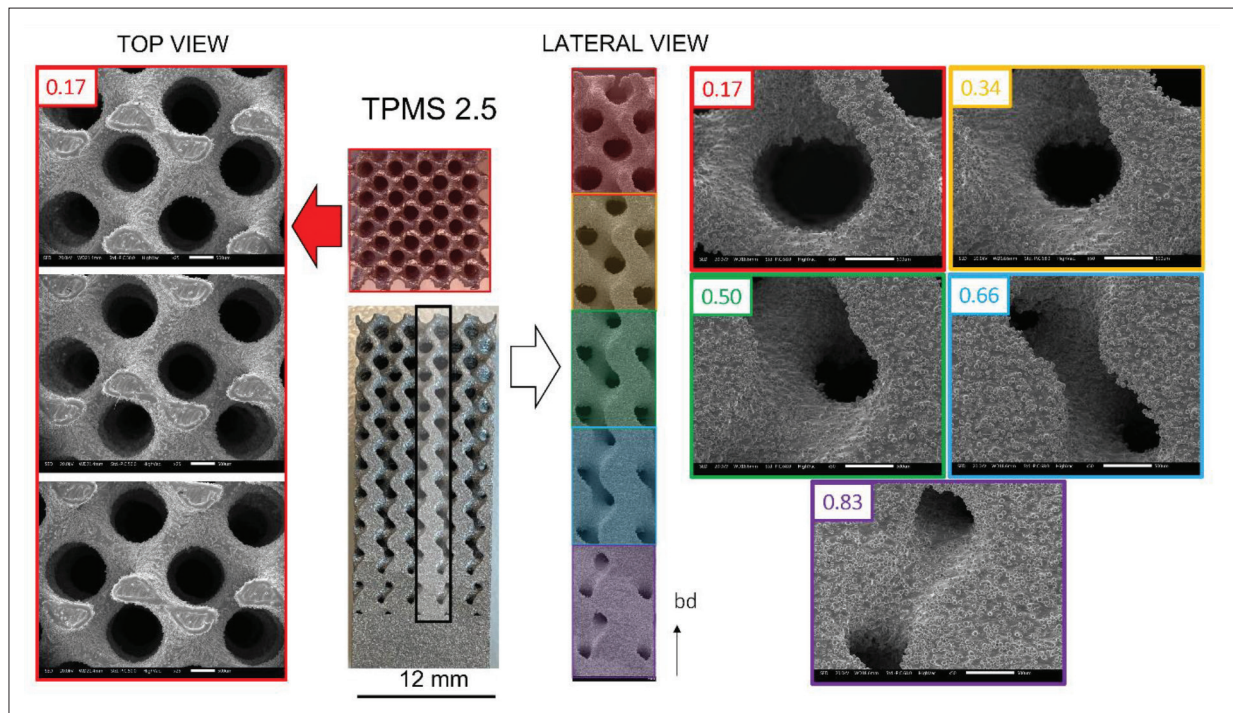
Figure 6. Top and lateral SEM views showing the details of the TPMS-FGPS 2.5.
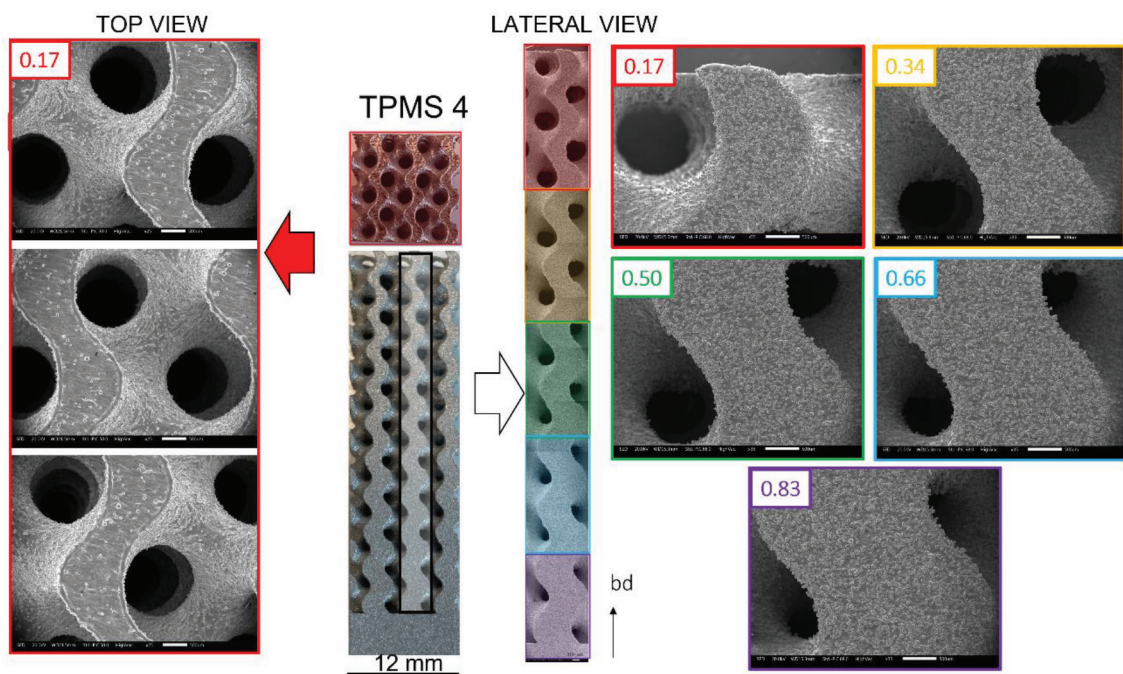

Figure 7. Top and lateral SEM views showing the details of the TPMS-FGPS 4.0.

size between SEM analysis and CAD are associated with the limitation of the 2D analysis. SEM micrographs were elaborated to estimate the diameter of the circumference that better approximates the pore boundary. This size was deemed to be more appropriate with respect to the diameter of the sphere inscribed inside the pore. Considering the ligament thickness, the undersizing effect may be correlated with a higher reduction of the ligament thickness in the middle part and the surface irregularity due to the printing process.

Table 4. Summary of the 2D metrological characterization of the TPMS-FGPS 2.5 and TPMS-FGPS 4.0 for the different relative density levels.

L (mm)	ρ_r CAD (–)	Ligament thickness CAD_max (mm)	Pore size CAD_max (mm)	Ligament thickness SEM (mm)[a]	Pore size SEM (mm)[a]	Ligament deviation to CAD (%)[a]	Pore deviation to CAD (%)[a]
2.5	0.17	0.73	1.74	0.61 ± 0.07	1.14 ± 0.03	−16 ± 10	−34 ± 2
	0.34	1.01	1.44	0.86 ± 0.13	0.84 ± 0.03	−15 ± 13	−42 ± 2
	0.50	1.27	1.20	1.15 ± 0.08	0.59 ± 0.02	−9 ± 6	−51 ± 2
	0.66	1.52	0.95	1.48 ± 0.17	0.32 ± 0.06	−3 ± 11	−66 ± 6
	0.83	1.82	0.66	1.74 ± 0.05	0.27 ± 0.03	−4 ± 3	−59 ± 5
4.0	0.17	1.43	2.38	1.30 ± 0.15	1.38 ± 0.14	−9 ± 10	−42 ± 6
	0.34	1.71	2.12	1.57 ± 0.14	1.15 ± 0.12	−8 ± 8	−46 ± 6
	0.50	1.96	1.88	1.87 ± 0.14	0.92 ± 0.11	−5 ± 7	−51 ± 6
	0.66	2.20	1.64	2.04 ± 0.10	0.67 ± 0.14	−7 ± 5	−63 ± 9
	0.83	2.47	1.36	2.31 ± 0.17	0.49 ± 0.06	−6 ± 7	−64 ± 4

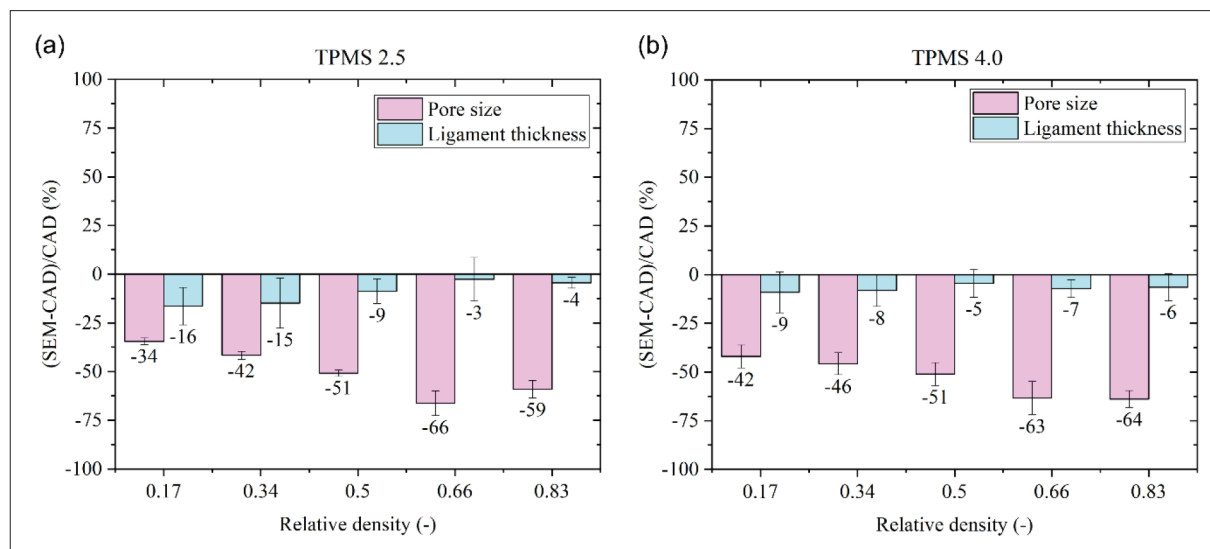[a] Data expressed as median ± MAD

Figure 8. CAD deviation using SEM analysis for (a) TPMS-FGPS 2.5 and (b) TPMS-FGPS 4.0.

μ-CT 3D images and details of the different relative density levels of both TPMS-FGPSs in terms of pore size, ligament thickness and overlap of CAD (yellow) on the μ-CT image (gray) in the case of TPMS-FGPS 2.5 and TPMS-FGPS 4.0 are shown in Figures 10 and 11, respectively. Considering the overlap details shown in Figure 10 (panels c, f, i, n, q) and Figure 11 (panels c, f, i, n, q), a higher amount of material and unmelted powder was observed in the upper part of the pores in the as-manufactured samples (gray arrows), and a variation of the ligament thickness due to printed process was detected (yellow arrows) in both TPMS-FGPSs. As demonstrated from Murchio *et al.*[67], the quality and accordance to the

CAD geometry depend on the printing angle, showing a tendency toward an elliptical cross-section shape by decreasing the printing angle from 90° to 0°. The superimposition of μ-CT image to the CAD shows good agreement between ligament inclination in the as-designed and as-manufactured samples, confirming the absence of geometrical distortions due to residual stresses. As-manufactured pore size and ligament thickness evaluated by means of the wall thickness method are summarized in Table 5 for both unit cell size conditions. As for the as-design samples, median + MAD is used as a value to evaluate pore size and ligament thickness. Figure 12 shows histograms of the percentage variations of pore size and
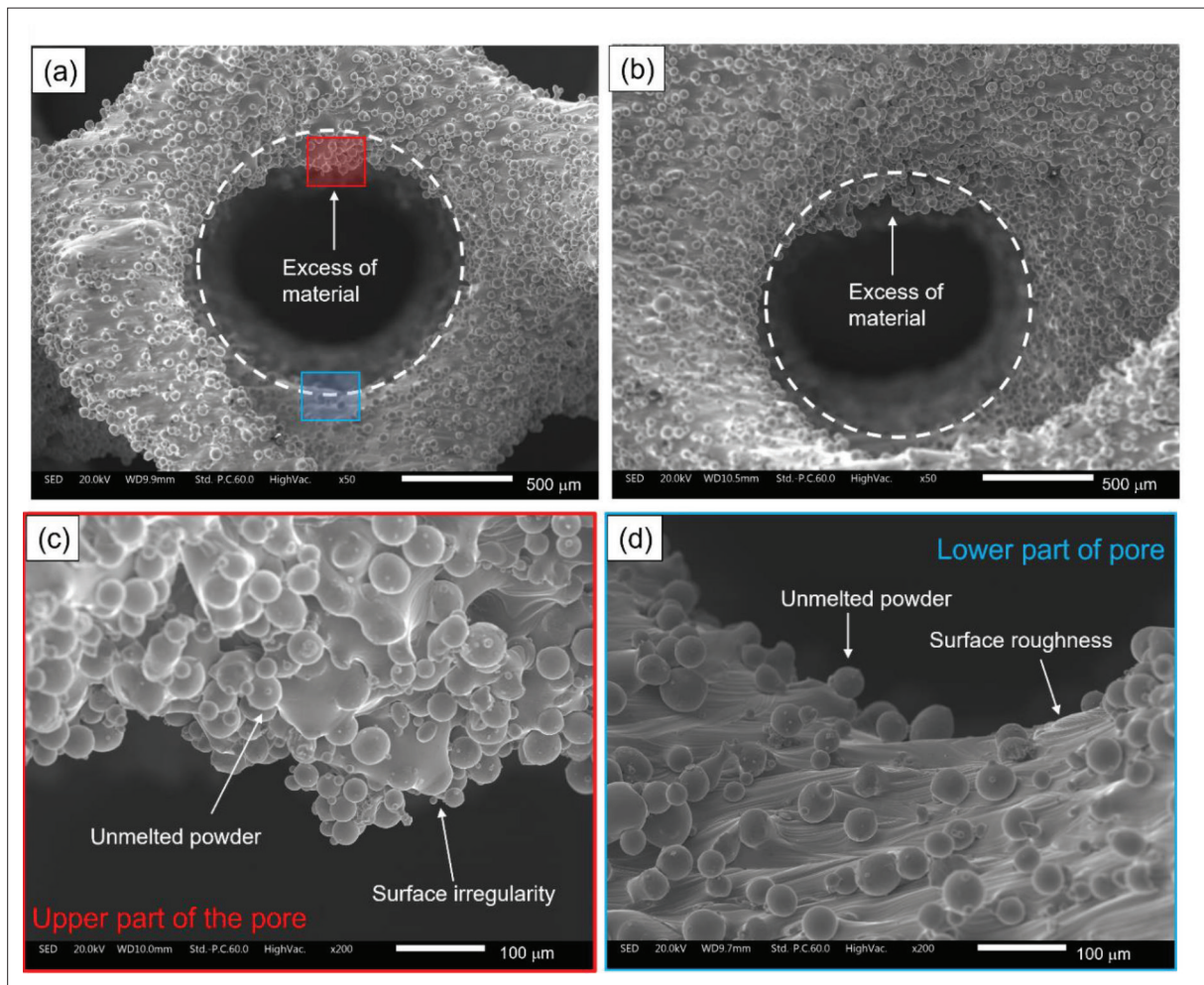
Figure 9. Detail of excess of material on pore surfaces for (a) TPMS-FGPS 2.5 and (b) TPMS-FGPS 4.0. Detail of the unmelted powder and of surface irregularity in the (c) upper and (d) lower parts of the pore.

ligament thickness obtained by comparing CAD with as-manufactured samples in the different relative density levels for both TPMS-FGPSs. Percentage variations of the as-manufactured sample to CAD underline a small undersizing of the ligament thickness and of the pore size after the printing. A maximum undersizing of the pore size of 5% and 2% and of the ligament of 4% and 3% was detected in TPMS-FGPS 2.5 and TPMS-FGPS 4.0, respectively, confirming the excellent overall quality of the AM process. To further justify the undersizing of both pore and ligament, overlap of as-designed (black) and as-manufactured (gray) samples in a simplified 2D view is shown in Figure 13. Surface irregularity, unmelted powder, and excess of material in the upper part of the pore lead to a lower pore size estimation with wall thickness method and to an overall reduced ligament thickness, as shown in Figure 13a and b for TPMS-FGPS 2.5 and TPMS-FGPS 4.0, respectively.

Figure 14 shows the percentage variation to CAD in the case of 2D (SEM) and 3D (μ-CT) metrological investigations. In both cases, an undersizing effect was detected in pore size and ligament thickness. Nevertheless, closer results were obtained in the case of the 3D characterization which gives more precise results thanks to the same method of analysis used in the as-designed and as-manufactured sample characterization (wall thickness method) and to the characterization of the entire volume. This did not occur in the case of 2D investigations, where only a portion of the sample was characterized.

3.2. Microstructural characterization
SEM micrograph details of the TPMS-FGPS 2.5 and TPMS-FGPS 4 are shown in Figure 15. Low magnification micrographs (Figure 15a for TPMS-FGPS 2.5 and Figure 15c for TPMS-FGPS 4.0) highlight the achievement of a near fully dense material and a columnar β grain
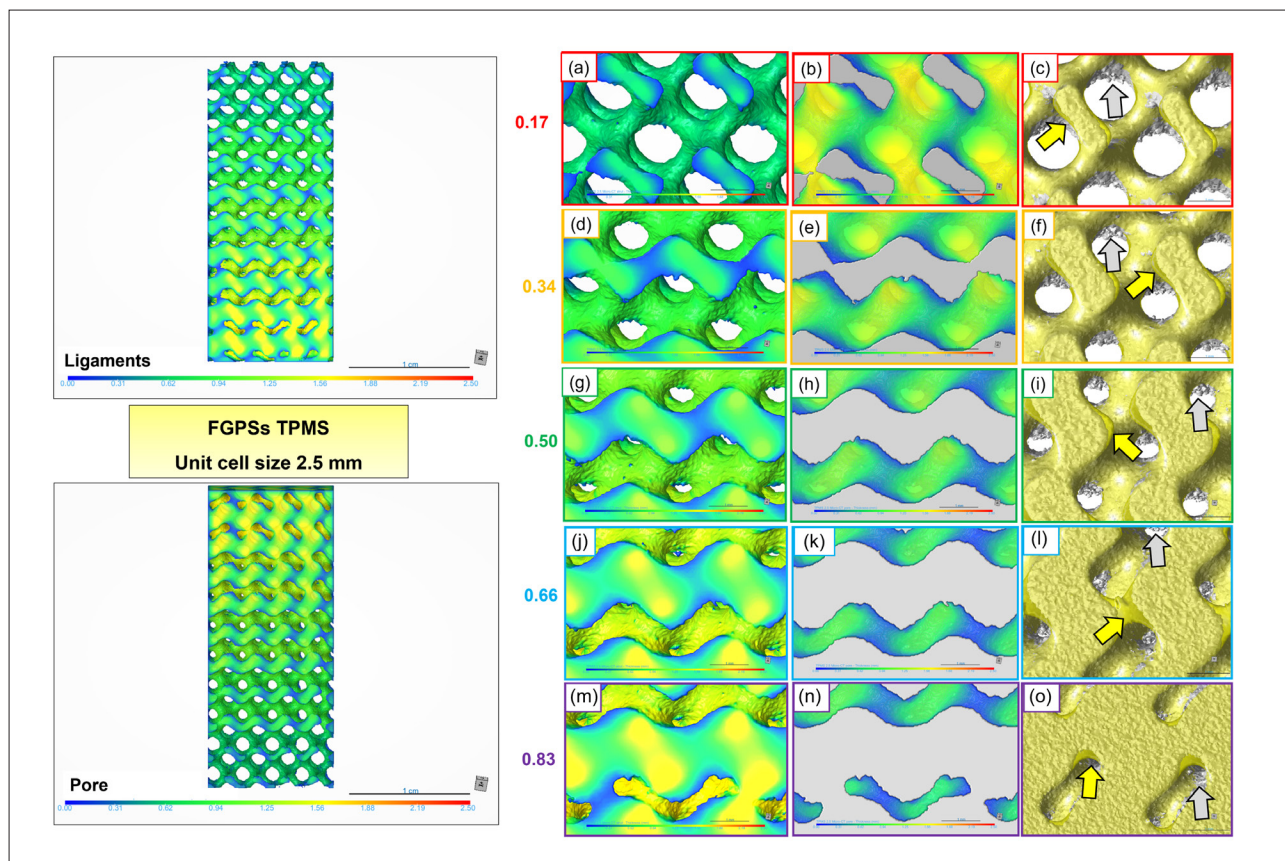
Figure 10. m-CT analysis of TPMS-FGPS 2.5 considering (a, d, g, j, m) ligament thickness, (b, e, h, k, n) pore size, and (c, f, i, l, o) m-CT image (gray) overlap with CAD (yellow) for the different relative densities.

structure oriented along the building direction. Higher magnification SEM micrographs shown in Figure 15b (TPMS-FGPS 2.5) and Figure 15c (TPMS-FGPS 4.0) emphasize the traces of melting pools and the epitaxial growth of β grain, which takes place along the heat flow direction. The epitaxial growth arose owing to partial remelting of previously consolidated layers and extended up to several millimeters in length, as shown in Figure 15a and c. The solidification structure and particularly the grain orientation are influenced by the local heat flow direction, which is almost parallel to the building direction[17,18]. Details of a lack of fusion defect due to insufficient overlap of successive melt pools is highlighted in Figure 15e[27]. Nevertheless, very few defects were detected highlighting the use of optimized process parameters. SEM analysis also evidenced the transition from planar to cellular structure at melt pool boundary, covering a region of around 0.5– 1 μm thickness inside the pool area (Figure 15d). This is attributed to the destabilization of the planar solidification front due to the constitutional undercooling inside the liquid ahead of the solid/liquid interface. In other words, planar to cellular transition occurs when the temperature

gradient inside the liquid becomes lower than the critical gradient inside the melting pool.

3.3. Quasi-static and cyclic compression tests

Quasi-static compression curves and examples of cyclic tests between 20% and 70% of yield stress are shown in Figure 16a and b. Three regions can be defined on the quasi-static compression curves: a linear elastic regime (i) until the yielding point, a plateau regime (ii) where the structure collapse takes place, and the final densification (iii) characterized by the positive slope of the curve. The collapse occurs in a progressive way, by buckling starting from the less stiff (lower relative density level) to the stiffer level (higher relative density level) up to complete densification of the FGPS[30]. Details of the structural deformation during the linear elastic, plateau, and densification regimes are shown in Figure 16c and d for TPMS-FGPS 2.5 and TPMS-FGPS 4.0, respectively. In both cases, the shape of the plateau regime and the collapse due to buckling highlight a bending-dominated behavior. Quasi-elastic modulus, namely the slope of the linear part of the curve, and yield stress at the 0.2% of deformation were calculated. Five
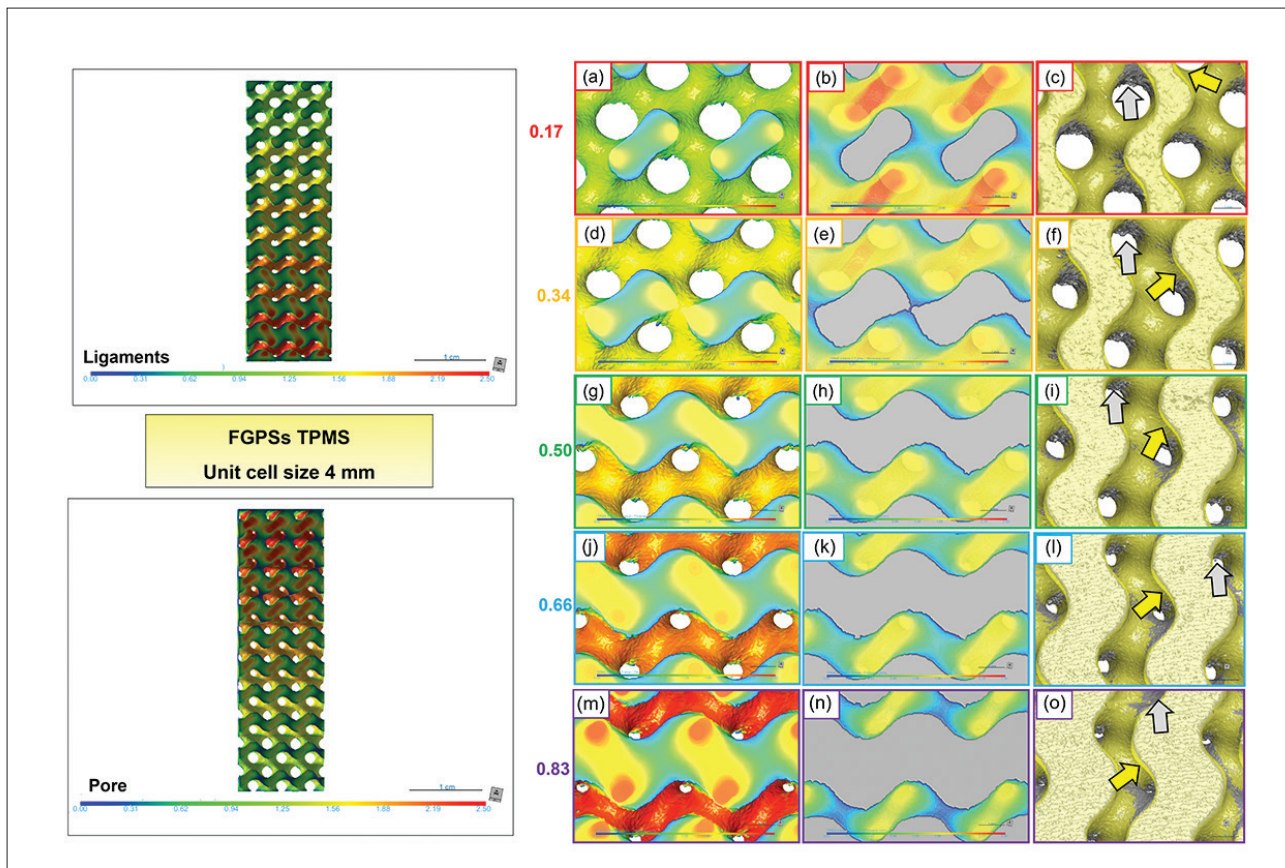
Figure 11. m-CT analysis of TPMS-FGPS 24.0 considering (a, d, g, j, m) ligament thickness, (b, e, h, k, n) pore size, and (c, f, i, l, o) m-CT image (gray) overlap with CAD (yellow) for the different relative densities.

Table 5. Summary of the 3D metrological characterization of the TPMS-FGPS 2.5 and TPMS-FGPS 4.0 for the different density relative levels.

L (mm)	ρ_r CAD (−)	Ligament thickness CAD_max (mm)	Pore size CAD_max (mm)	Ligament thickness μ-CT_max	Pore size μ-CT_max 1(mm)	Ligament deviation to CAD (%)	Pore deviation to CAD (%)
2.5	0.17	0.73	1.74	0.70	1.68	−4	−3
	0.34	1.01	1.44	0.98	1.43	−3	−1
	0.50	1.27	1.20	1.23	1.16	−3	−3
	0.66	1.52	0.95	1.48	0.92	−3	−3
	0.83	1.82	0.66	1.79	0.63	−2	−5
4.0	0.17	1.43	2.38	1.39	2.36	−3	−1
	0.34	1.71	2.12	1.67	2.1	−2	−1
	0.50	1.96	1.88	1.89	1.85	−4	−2
	0.66	2.20	1.64	2.13	1.62	−3	−1
	0.83	2.47	1.36	2.4	1.36	−3	0

loading-unloading cycles between 20% and 70% of the yield stress (working in the elastic deformation regime) are necessary to stabilize the mechanical behavior owing to the poor stability of the cellular structures during the first loading cycle, especially in the case of high porosity[68].

This is highlighted by the slope that changes after the first loading-unloading cycle and remains constant in the subsequent four cycles. The average elastic modulus obtained after stabilization is the E cyclic. The $E_{quasi-elastic}$, the yield stress, and the E_{cyclic} are reported in Table 6. Higher
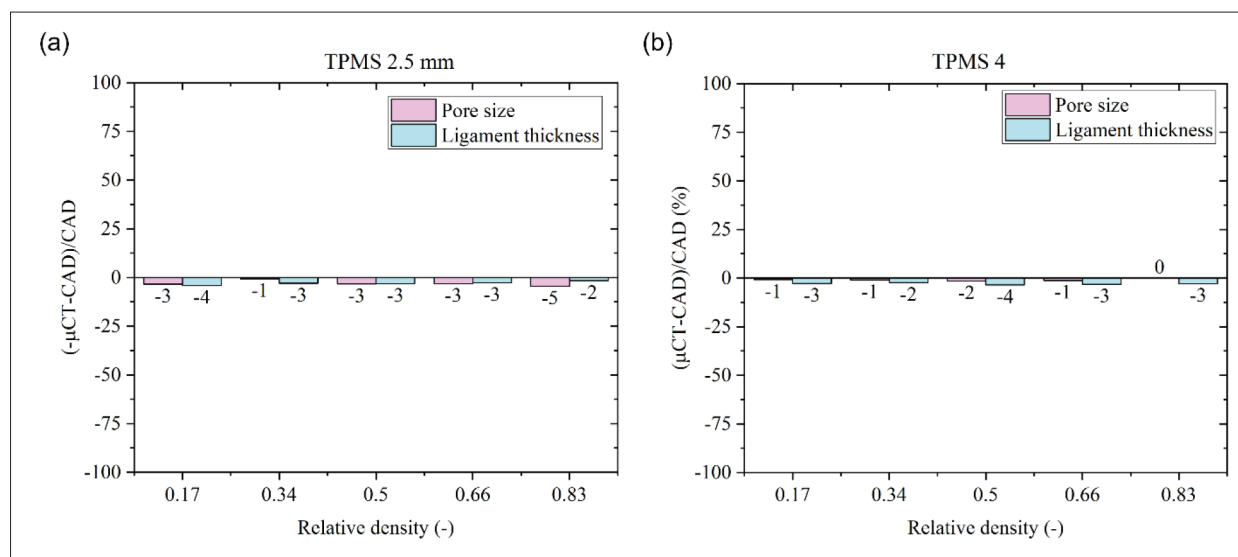
Figure 12. CAD deviation using μ-CT analysis for (a) TPMS-FGPS 2.5 and (b) TPMS-FGPS 4.0.
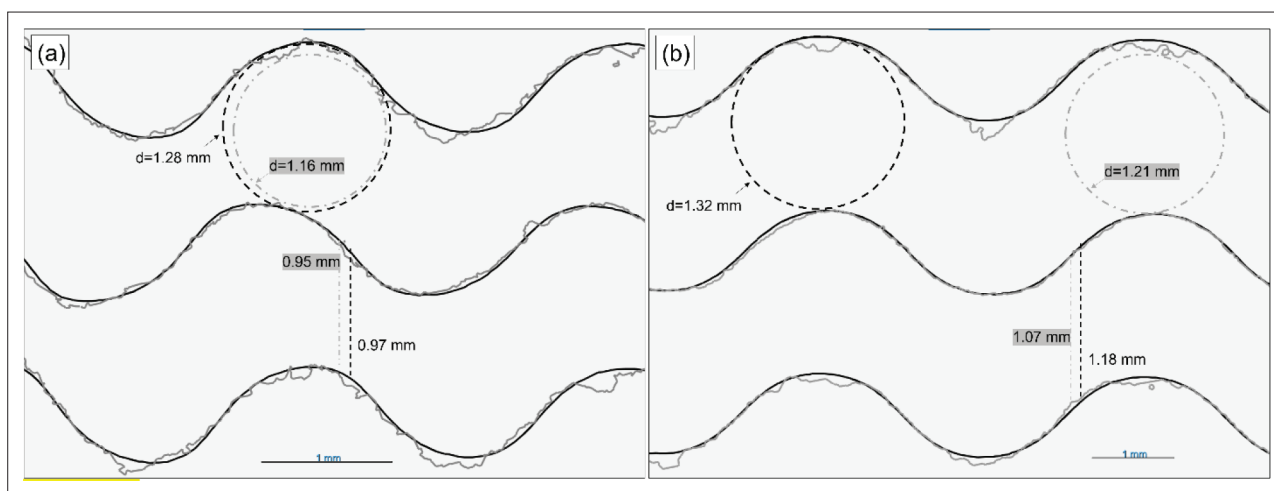

Figure 13. Influence of the surface irregularities on the pore and ligament thickness analysis in a simplified 2D view overlapping CAD (black) with μ-CT scan (gray) for (a) TPMS-FGPS 2.5 and (b) TPMS-FGPS 4.0.

values of the elastic modulus were observed by comparing the $E_{quasi-elastic}$ with the E_{cyclic} since the achievement of the mechanical stabilization after a preload. This is also evident by noting the slopes of the stress-strain curves in Figure 16b that increase from the first (equal to the $E_{quasi-elastic}$) to the second cycle and reaches a plateau. During the first loading cycle, a major part of the structure was loaded in the elastic regime. Nevertheless, localized plastic deformation occurred at the junction between the ligament, leading to a nonhomogenous distribution of the strain field. With the subsequent load, the elastic regime was extended by strain hardening, leading to a higher stiffness[61]. After the first loading condition, the elastic modulus remained constant, highlighting the stabilization of the preload. The compression yield strength of both TPMS-FGPS was higher

than the one of the trabecular bone (0.8–11.6 MPa)[34]. In TPMS-FGPS 2.5, a stabilized elastic modulus of 4.1 GPa was obtained, in line with the cancellous bone, while that of TPMS-FGPS 4.0 is around 10.7 GPa, which is closer to the cortical part of the bone. Nevertheless, considering the Gibson–Ashby equation, i.e., Equation I, such large difference between the elastic moduli of TPMS-FGPS 2.5 and TPMS-FGPS 4.0 is not justified since the structures are characterized by the same relative densities.

To explain this result, a simulation was carried out to calculate the elastic modulus of the different density levels. Numerical homogenization method was performed in the case of the as-designed (E_{nom}^{hom}) and the as-manufactured (E_{real}^{hom}) ligament thickness. The as-designed and the as-
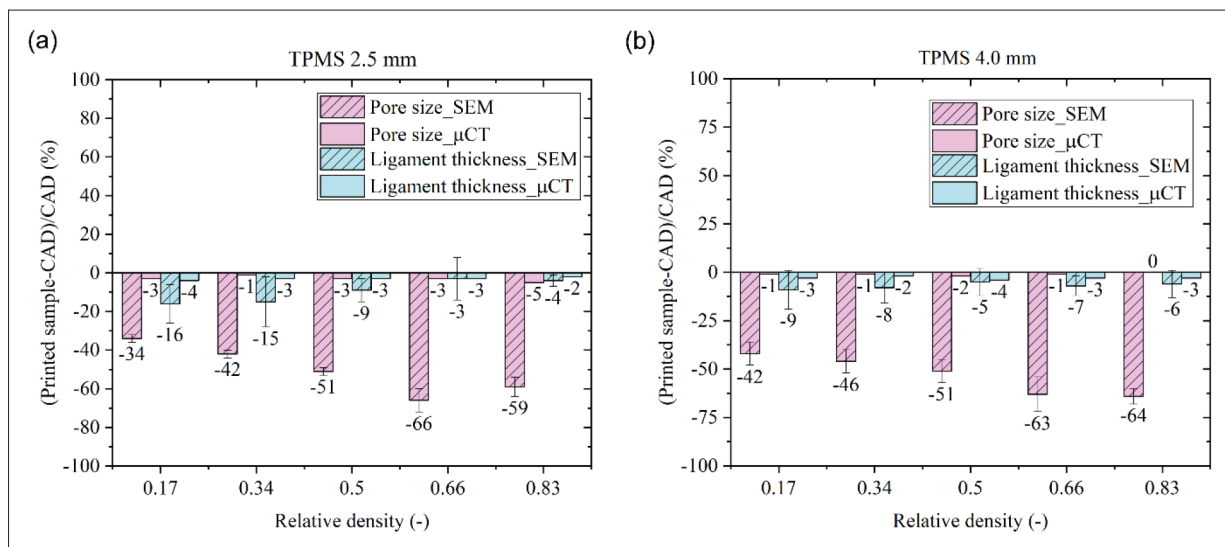
Figure 14. Comparison between 2D and 3D characterizations in the case of (a) TPMS-FGPS 2.5 and (b) TPMS-FGPS 4.0.

manufactured thickness values were used to calculate the homogenized properties for each cell dimension and density level using the software nTopology (nTopology Inc., USA). Since the design of the TPMS unit cell size was done by means of the implicit Equation V, the calculation of the real level constant "t" by means of the as-manufactured ligament thickness is necessary. Equations XIII and XIV, obtained by CAD data, were used to calculate the corresponding level constant "t" in the case of as-manufactured ligament thickness of TPMS-FGPS 2.5 and TPMS-FGPS 4.0, respectively.

$$t_{2.5} = -0.7572 + 0.1842l_t + 0.4998l_t^2 - 0.1365l_t^3$$
$$Adj\ R^2 = 0.99982X \qquad \text{XIII}$$

$$t_{4.0} = -1.1454 - 0.8071l_t + 1.0483l_t^2 - 0.1723l_t^3$$
$$Adj\ R^2 = 0.99995 \qquad \text{XIV}$$

The results are summarized in Table 7. Lower level constants were achieved in the case of as-manufactured samples due to the undersizing effect caused by the 3D printing process. Finite element analysis was performed to compute the homogenized material properties[64,65]. Table 8 shows the elastic modulus obtained by the homogenization in the case of as-designed (E_{nom}^{hom}) and as-manufactured (E_{real}^{hom}) samples. Elastic modulus values of the different relative density levels in the case of 2.5 mm and 4.0 mm unit cell size are obtained as demonstrated by the Gibson–Ashby equation, i.e., Equation I. Therefore, no influence of the unit cell size was detected for the same relative density level. In other words, the elastic modulus of a porous structure is affected by the type of cellular structure, the bulk material, and the relative density. As shown in Equation I, an increased relative density leads to an increased elastic modulus.

A more accurate analysis was obtained, considering the as-manufactured ligament thickness (E_{real}^{hom}).

To define the overall elastic modulus of both TPMS-FGPSs, the stiffness values reported in Table 8 were input into Equation III, and the obtained numerical values are summarized in Table 9 along with the experimental E_{cyclic}.

The theoretical values obtained by means of the homogenization method and Equation III lead to a discrepancy from the experimental values of around 10% and −8% considering the as-designed and the as-manufactured ligament thickness of TPMS-FGPS 2.5. Good correlation in both conditions, namely using CAD and as-printed values, was resulted owing to the small geometric deviation from as-manufactured sample and CAD shown through 3D metrological characterization. In addition, a result close to the experimental values was obtained, highlighting the promising ability of the homogenization simulation to reduce the number of experimental trials and consequently the time consumption to evaluate the elastic modulus of a designed and printed cellular structure. Different results were observed in the case of TPMS-FGPS 4 where a large significant undersizing (−61% and −79%) was obtained, considering both the as-designed and as-manufactured ligament thickness with respect to the experimental results. The homogenization method relies on the hypothesis of an infinite cell repetition in space. In the TPMS 4.0, the specimen has a limited number of unit cells: 3 × 3 unit cells on the normal area with respect to the load, meaning along x and y directions. This deeply influences the degree of accuracy the homogenized model is able to achieve, since the effect given by the edge effect is non-negligible[64,69,70]. In order to highlight the importance of the number of unit
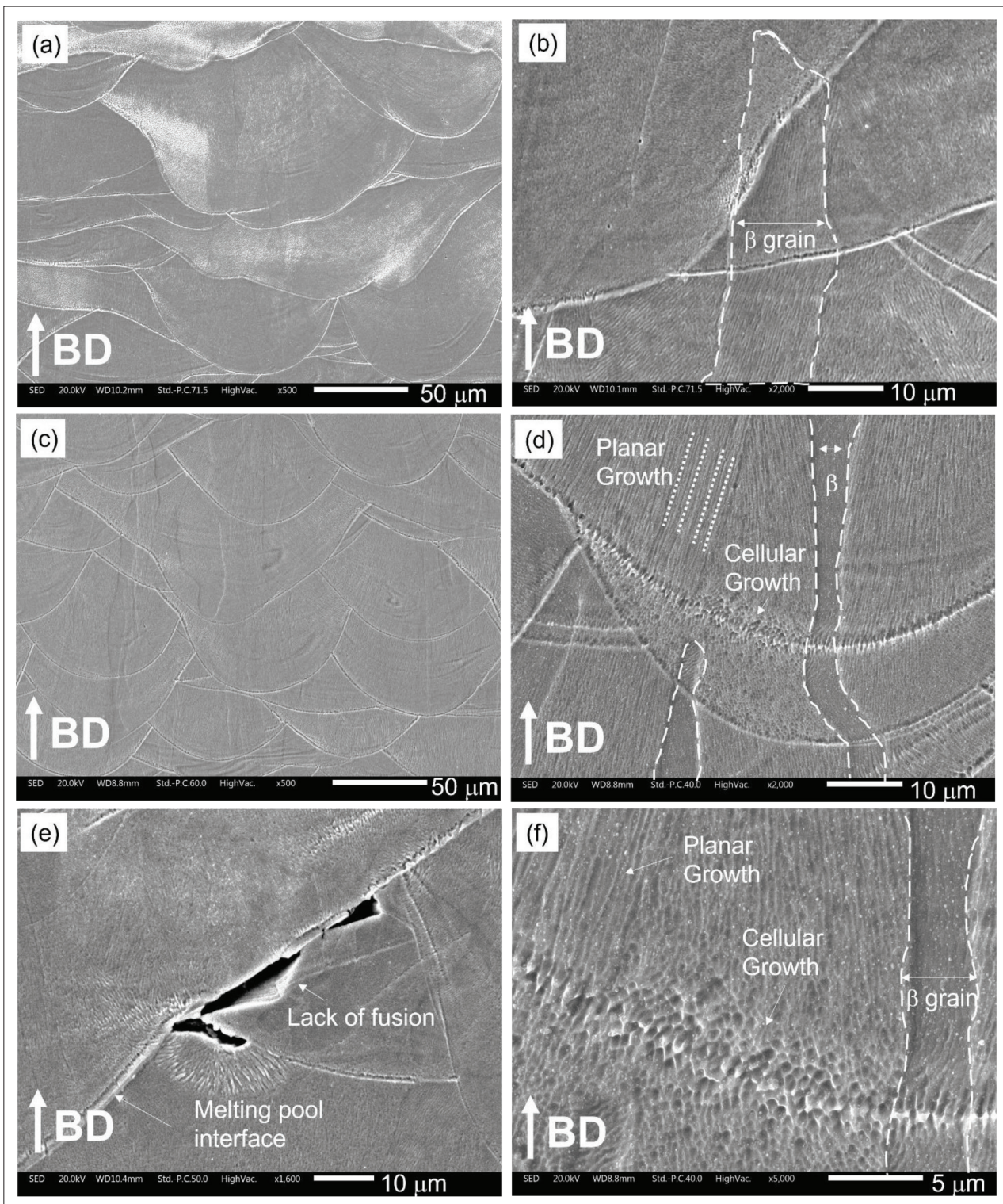
Figure 15. SEM micrographs at different magnifications for (a, b) TPMS-FGPS 2.5 and (c, d) TPMS-FGPS 4.0. (e) Detail images of a lack-of-fusion defect and (f) of the planar to cellular growth transition.
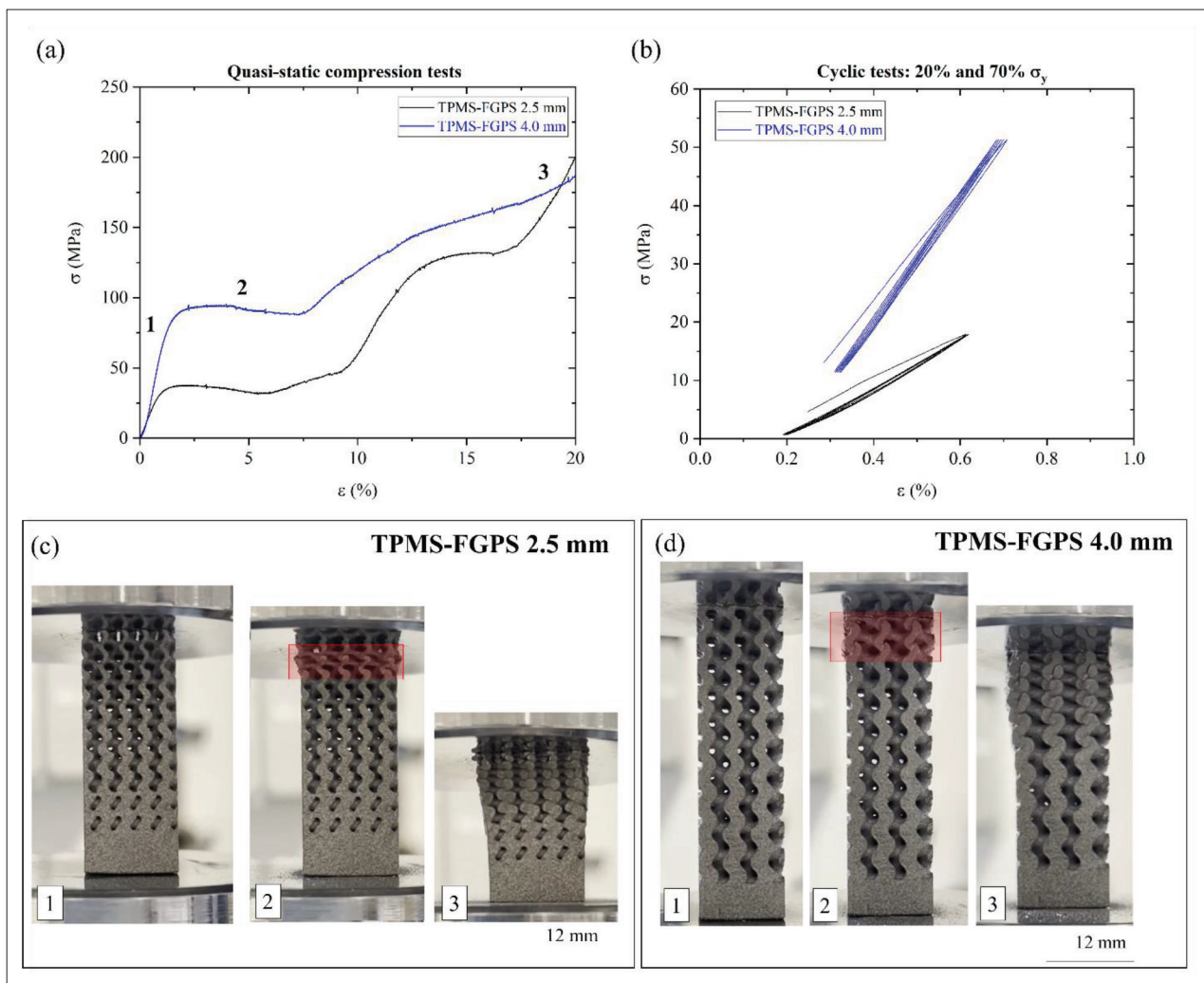
Figure 16. (a) Quasi-static compression curves and (b) cyclic curves between 20% and 70% of the yield stress for both TPMS-FGPSs. (c, d) Details of the collapses observed at different stages of quasi-static compression curves of both TPMS-FGPSs.

Table 6. Summary of the quasi-elastic modulus and yield stress of the two TPMS-FGPSs.

TPMS FGPSs	$E_{quasi\text{-}elastic}$ (GPa)	σ_y (MPa)	E_{cyclic} (GPa)
2.5 mm	3.5 ± 0.4	33.4 ± 0.4	4.1 ± 0.1
4.0 mm	7.1 ± 0.2	84.3 ± 0.1	10.7 ± 0.1

Table 7. Summary of the real level constant (t) associated to the ligament thickness of the as-manufactured samples for both TPMS FGPSs.

| TPMS	2.5 mm		4.0 mm	
ρ_r CAD (−)	Ligament thickness μ-CT_max (mm)	Level constant (t) (−)	Ligament thickness μ-CT_max (mm)	Level constant (t) (−)
0.17	0.70	−0.43	1.56 ± 0.18	−0.70
0.34	0.98	−0.23	1.38 ± 0.06	−0.48
0.50	1.23	−0.03	1.15 ± 0.05	−0.09
0.66	1.48	0.17	0.92 ± 0.03	0.23
0.83	1.79	0.39	0.64 ± 0.02	0.57

Table 8. Summary of Young's modulus obtained by means of homogenization method on the single unit cell for both TPMS structures (nTopology software).

TPMS-FGPSs	Relative density ρ_r (–)	E_{nom}^{hom} (GPa)	E_{real}^{hom} (GPa)
2.5 mm	0.17	1.15	0.93
	0.34	4.88	4.16
	0.50	10.83	9.77
	0.66	19.47	18.00
	0.83	32.5	31.13
4.0 mm	0.17	1.12	0.86
	0.34	4.88	2.79
	0.50	10.84	8.92
	0.66	19.47	16.73
	0.83	32.7	28.67

Table 9. Elastic modulus of the two TPMS-FGPSs obtained by experimental analysis and through homogenization using nominal and real ligament dimensions one.

TPMS-FGPSs	E_{cyclic} (GPa)	E_{nom}^{hom} (GPa)	E_{real}^{hom} (GPa)
2.5 mm	4.1 ± 0.1	4.6 (10%)	3.8 (−8%)
4.0 mm	10.7 ± 0.1	4.2 (−61%)	3.1 (−70%)

cell size on the normal plane in the case of homogenization analysis, a fully solid FEA of the complete specimen with 4.0 mm and 2.5 mm unit cell size were performed, as shown in Figures 17 and 18, respectively. Thanks to Equation XII, an elastic modulus of 7.7 GPa and of 3.2 GPa was obtained in the case of TPMS-FGPS 4.0 and TPMS-FGPS 2.5, respectively. The stiffness obtained in case of TPMS-FGPS 4 is closer to the experimental value (−25%), confirming that the non-negligible edge effects occur in the case of a small number of unit cells in the normal area with respect to the load[64,69,70]. A similar variation with respect to experimental results was achieved with TPMS-FGPS 2.5 (−27%). The deviation of approximately 25% between the experimental and predicted elastic modulus through FEA may be attributed to the fact that compression testing is not an ideal quasi-static process, even at low strain rates. As noted by Yang *et al.*[71], the ideal quasi-static compression test occurs primarily in the first layers near the applied load, where the stress is not transmitted to lower parts. The solid FEA analysis presented here was conducted to highlight the limitations of the homogenization method when the minimum required number of unit cell sizes was not used. Further considerations, deriving from more detailed FEA modeling, will be the subject of future works. Taken together, the measurement of the Gibson–Ashby constants was carried out in the case of TPMS-FGPS 2.5 since it was characterized by enough unit cell number to avoid the edge effects (Figure 19). The plot permits to
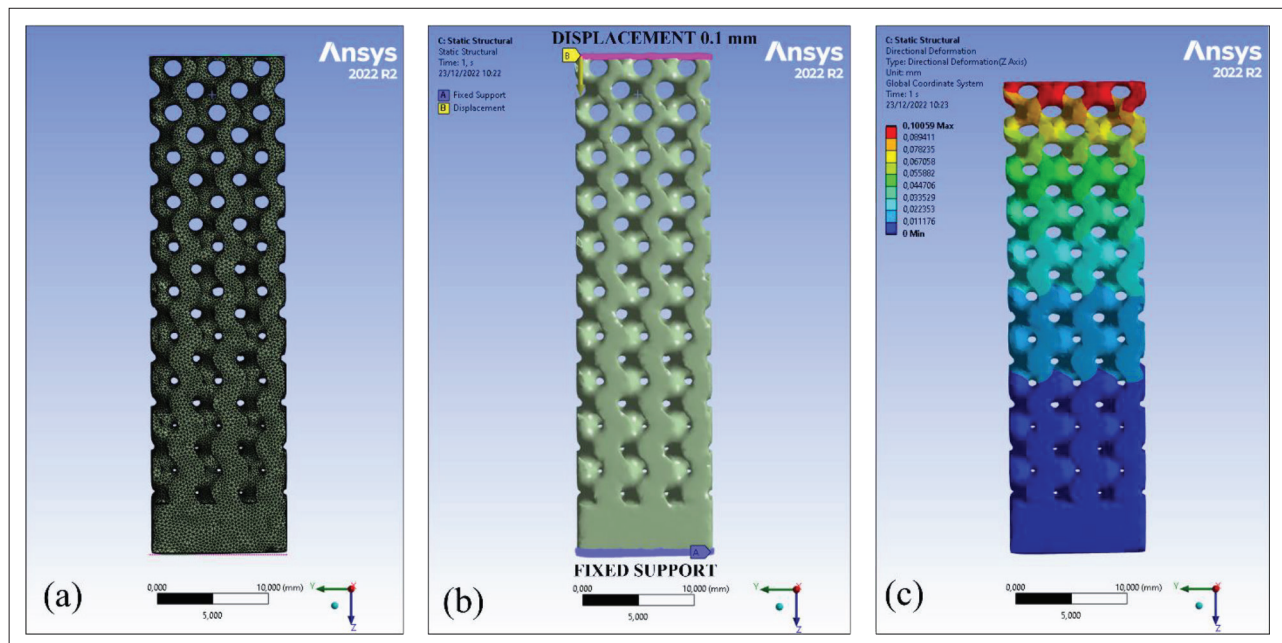
Figure 17. Finite element simulation of the complete TPMS-FGPS 4.0. (a) The contour mesh of the as-manufactured samples. (b) Loading condition resembling the experimental condition, i.e., a fixed constraint on the bottom surface of the specimen and a fixed displacement equal to 0.1 mm in the vertical direction on the top surface. (c) Results of the simulation analysis.

Figure 18. Finite element simulation of the complete TPMS-FGPS 2.5. (a) The contour mesh of the as-manufactured samples. (b) Loading condition resembling the experimental condition, i.e., a fixed constraint on the bottom surface of the specimen and a fixed displacement equal to 0.1 mm in the vertical direction on the top surface. (c) Results of the simulation analysis.
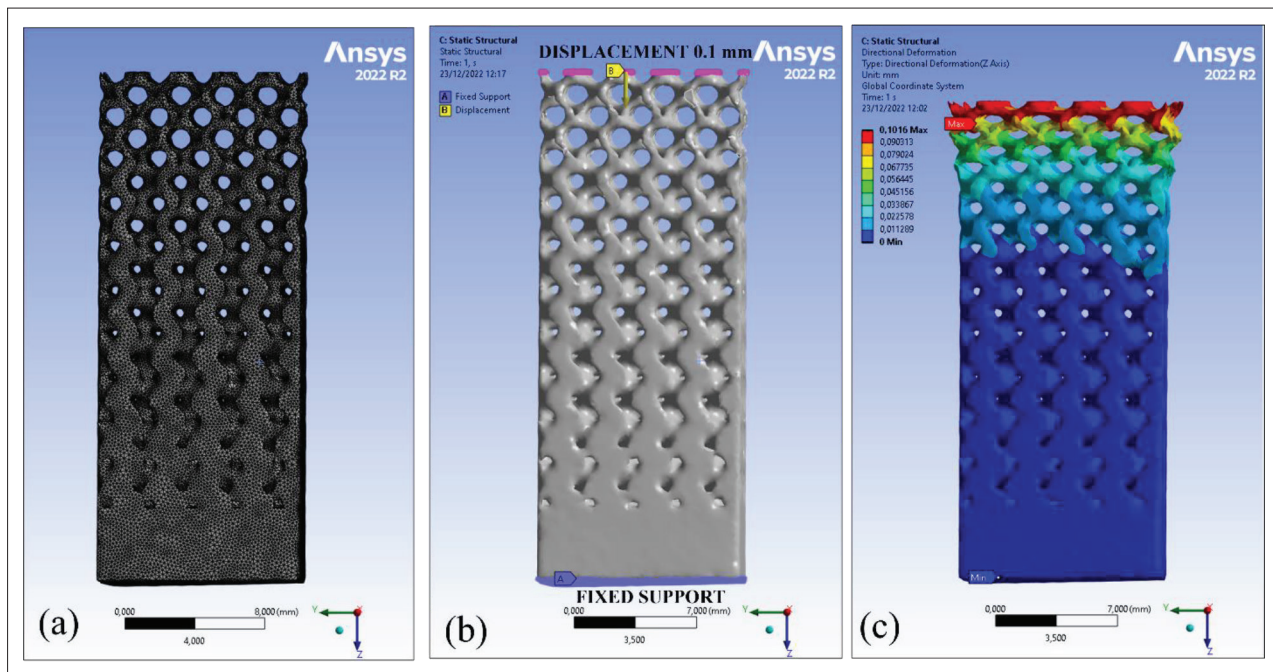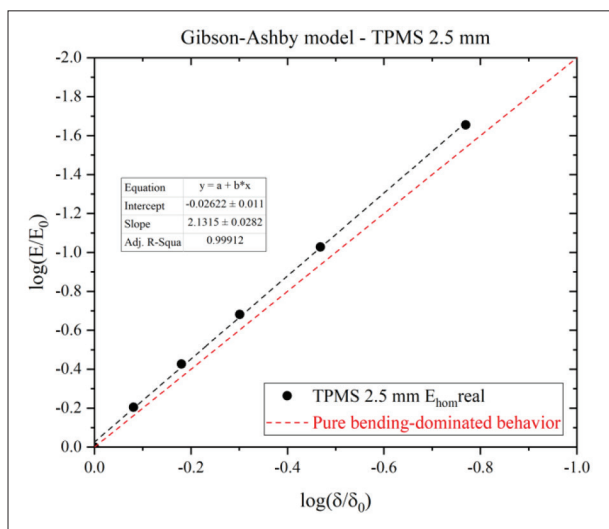

Figure 19. Gibson–Ashby fitting equation for TPMS with 2.5 mm of unit cell size.

obtain C_1 equal to 0.94 and n_1 equal to 2.13, as found by other authors[36,73]. The exponential constants are very close to the pure bending-dominated behavior, as shown by the comparison with the red curve in Figure 19.

4. Conclusion

2D and 3D metrological characterizations were performed on two different 3D-printed TPMS-FGPSs

with unit cell sizes of 2.5 and 4.0 mm, and relative density gradients of 0.17, 0.34, 0.50, 0.66, and 0.83. Quasi-static and cyclic compression tests were carried out to evaluate $E_{quasi-elastic}$, yield stress and E_{cyclic}. Homogenization analysis and simple lumped model were conducted, and the obtained results were compared with the experimental values. FEA further explained the discrepancy observed between experimental simulated values in the case of TPMS-FGPS 4.0. The main results of the study are summarized as follows.

(i) 2D metrological characterization by SEM highlights an undersizing of both ligament and pore size with a maximum variation of 16% (TPMS-FGPS 2.5) and 9% (TPMS-FGPS 4.0) and of 66% (TPMS-FGPS 2.5) and 64% (TPMS-FGPS 4.0), respectively. The undersizing of the pore and ligament with respect to the CAD can be attributed to an excess of material, a higher amount of unmelted powder in the upper part of the pores, and variations in the diameter of the ligament.

(ii) 3D metrological characterization by X-ray and μ-CT imaging shows an undersizing of both the pore size and ligament thickness, which is lower than 5% in TPMS-FGPS 2.5 and TPMS-FGPS 4.0, confirming the excellent printability of these structures.

(iii) The 3D metrological characterization by means of μ-CT imaging permits a more holistic evaluation

of the printability of the TPMS-FGPSs thanks to the analysis of the entire volume and to the use of the same method (wall thickness method) to characterize the as-designed and printed samples.

(iv) The compression yield strength of both TPMS-FGPS results is higher than that of the trabecular bone (0.8–11.6 MPa). The E_{cyclic} of TPMS-FGPS 2.5 (4.1 GPa) resumes that of the cancellous bone, while the E_{cyclic} of TPMS-FGPS 4.0 (10.7 GPa) is in line with that of the cortical bone.

(v) A simulation analysis by means of homogenization method and simple lumped model confirms that the discrepancy between CAD and experimental dimensions could be ascribed to edge effects, which are not negligible when the number of unit cells is too low as in the case of TPMS-FGPS 4.0.

(vi) The values the Gibson–Ashby constants highlight the bending-dominated behavior exhibited by the TPMS-FGPS 2.5.

Acknowledgments

Funding

Conflict of interest

The authors declare that they have no known financial interests or personal relationships that could have appeared to influence the work reported in this paper. Alireza Jam is currently with the National Center for Additive Manufacturing Excellence (NCAME) at Auburn University.

Author contributions

Conceptualization: Lorena Emanuelli
Methodology: Lorena Emanuelli, Raffaele De Biasi, Anton du Plessis, Matteo Benedetti, Massimo Pellizzari
Investigation: Lorena Emanuelli, Raffaele De Biasi, Carlo Lora, Alireza Jam
Writing – original draft: Lorena Emanuelli, Raffaele De Biasi, Anton du Plessis, Matteo Benedetti, Massimo Pellizzari
Writing – review & editing: All authors

Ethics approval and consent to participate

Not applicable.

Consent for publication

Not applicable.

Availability of data

No additional data are available to the public.

References

1. Sam Froes FH, Qian M, Niinomi M, 2019, *Titanium for Consumer Applications: Real World Use of Titanium*, 1–349.

   https://doi.org/10.1016/C2017-0-03513-9

2. Balakrishnan P, Sreekala MS, Thomas S, 2018, *Fundamental Biomaterials: Metals*, 1–450.

   https://doi.org/10.1016/C2016-0-03502-7

3. Standard Specification for Wrought Titanium-6Aluminum-4Vanadium ELI (Extra Low Interstitial) Alloy for Surgical Implant Applications (UNS R56401).

   https://www.astm.org/f0136-13r21e01.html (accessed December 7, 2022).

4. Geetha M, Singh AK, Asokamani R, *et al.*, 2009, Ti based biomaterials, the ultimate choice for orthopaedic implants: A review. *Prog Mater Sci*, 54:397–425.

   https://doi.org/10.1016/J.PMATSCI.2008.06.004

5. Rao S, Ushida T, Tateishi T, *et al.*, 1996, Effect of Ti, Al, and V ions on the relative growth rate of fibroblasts (L929) and osteoblasts (MC3T3-E1) cells. *Biomed Mater Eng*, 6:79–86.

   https://doi.org/10.3233/BME-1996-6202

6. Wang M, Lin F, Zhang X, *et al.*, 2022, Combination of alpinia oxyphylla fructus and schisandra chinensis fructus ameliorates aluminum-induced Alzheimer's disease via reducing BACE1 expression. *J Chem Neuroanat*, 126: 102180.

   https://doi.org/10.1016/J.JCHEMNEU.2022.102180

7. Abdel-Hady Gepreel M, Niinomi M, 2013, Biocompatibility of Ti-alloys for long-term implantation. *J Mech Behav Biomed Mater*, 20:407–415.

   https://doi.org/10.1016/J.JMBBM.2012.11.014

8. Kumar A, Nune KC, Misra RDK, 2016, Biological functionality and mechanistic contribution of extracellular matrix-ornamented three dimensional Ti-6Al-4V mesh scaffolds. *J Biomed Mater Res Part A*, 104:2751–2763.

   https://doi.org/10.1002/JBM.A.35809.

9. ASTM F2066-18 - Standard Specification for Wrought Titanium-15 Molybdenum Alloy for Surgical Implant Applications (UNS R58150).

10. ASTM F1813-21 - Standard Specification for Wrought Titanium-12Molybdenum-6Zirconium-2Iron Alloy for Surgical Implant (UNS R58120).

11. ISO - ISO 5832-14:2019 - Implants for surgery—Metallic materials—Part 14: Wrought titanium 15-molybdenum 5-zirconium 3-aluminium alloy.

12. Brunke F, Siemers C, Rösler J, 2020, Second-generation titanium alloys Ti-15Mo and Ti-13Nb-13Zr: A comparison of the mechanical properties for implant applications. *MATEC Web Conf*, 321:05006.

https://doi.org/10.1051/matecconf/202032105006

13. Duan R, Li S, Cai B, *et al.*, 2021, A high strength and low modulus metastable β Ti-12Mo-6Zr-2Fe alloy fabricated by laser powder bed fusion in-situ alloying. *Addit Manuf*, 37:101708.

https://doi.org/10.1016/j.addma.2020.101708

14. Escobar Claros CA, Contri Campanelli L, Moreira Jorge A, *et al.*, 2021, Corrosion behaviour of biomedical β-titanium alloys with the surface-modified by chemical etching and electrochemical methods. *Corros Sci*, 188:109544.

https://doi.org/10.1016/J.CORSCI.2021.109544

15. *Materials Properties Handbook: Titanium Alloys*, ASM International.

https://www.asminternational.org/materials-resources/results/-/journal_content/56/10192/06005G/PUBLICATION (accessed 13 July 2022).

16. Macias-Sifuentes MA, Xu C, Sanchez-Mata O, *et al.*, 2021, Microstructure and mechanical properties of β-21S Ti alloy fabricated through laser powder bed fusion. *Prog Addit Manuf*, 6:417–430.

https://doi.org/10.1007/s40964-021-00181-7

17. Pellizzari M, Jam A, Tschon M, *et al.*, 2020, A 3D-printed ultra-low young's modulus β-Ti alloy for biomedical applications. *Materials (Basel)*, 13:1–16.

https://doi.org/10.3390/ma13122792

18. Jam A, du Plessis A, Lora C, *et al.*, 2022, Manufacturability of lattice structures fabricated by laser powder bed fusion: A novel biomedical application of the beta Ti-21S alloy. *Addit Manuf*, 50:102556.

https://doi.org/10.1016/J.ADDMA.2021.102556

19. Gibson LJ, Ashby MF, Harley BA, *Cellular Materials in Nature and Medicine*, 309.

20. Ashby MF, 2006, The properties of foams and lattices. *Philos Trans R Soc A Math Phys Eng Sci*, 364:15–30.

https://doi.org/10.1098/RSTA.2005.1678

21. Abate KM, Nazir A, Jeng JY, 2021, Design, optimization, and selective laser melting of vin tiles cellular structure-based hip implant. *Int J Adv Manuf Technol*, 112:2037–2050.

https://doi.org/10.1007/S00170-020-06323-5

22. Stewart C, Akhavan B, Wise SG, *et al.*, 2019, A review of biomimetic surface functionalization for bone-integrating orthopedic implants: Mechanisms, current approaches, and future directions. *Prog Mater Sci*, 106:100588.

https://doi.org/10.1016/j.pmatsci.2019.100588

23. Bobbert FSL, Lietaert K., Eftekhari AA, *et al.*, 2017, Additively manufactured metallic porous biomaterials based on minimal surfaces: A unique combination of topological, mechanical, and mass transport properties. *Acta Biomater*, 53:572–584.

https://doi.org/10.1016/j.actbio.2017.02.024

24. Zhang J, Chen X, Sun Y, *et al.*, 2022, Design of a biomimetic graded TPMS scaffold with quantitatively adjustable pore size. *Mater Des*, 218:110665.

https://doi.org/10.1016/J.MATDES.2022.110665

25. Zheng Y, Han Q, Wang J, *et al.*, 2020, Promotion of osseointegration between implant and bone interface by titanium alloy porous scaffolds prepared by 3D printing. *ACS Biomater Sci Eng*, 6:5181–5190.

https://doi.org/10.1021/acsbiomaterials.0c00662

26. Al-Ketan O, Rowshan R, Abu Al-Rub RK, 2018, Topology-mechanical property relationship of 3D printed strut, skeletal, and sheet based periodic metallic cellular materials. *Addit Manuf*, 19:167–183.

https://doi.org/10.1016/J.ADDMA.2017.12.006

27. Tang M, Pistorius PC, Beuth JL, 2017, Prediction of lack-of-fusion porosity for powder bed fusion. *Addit Manuf*, 14:39–48.

https://doi.org/10.1016/J.ADDMA.2016.12.001

28. Alaña M, Cutolo A, Probst G, *et al.*, 2020, Understanding elastic anisotropy in diamond based lattice structures produced by laser powder bed fusion: Effect of manufacturing deviations. *Mater Des*, 195:1–12.

https://doi.org/10.1016/j.matdes.2020.108971

29. Emanuelli L, Jam A, Du Plessis A, *et al.*, Manufacturability of functionally graded porous β-Ti21S auxetic architected biomaterials produced by laser powder bed fusion: Comparison between 2D and 3D metrological characterization. *Int J Bioprint,* 9(2): 0213.

30. Benedetti M, du Plessis A, Ritchie RO, *et al.*, 2021, Architected cellular materials: A review on their mechanical properties towards fatigue-tolerant design and fabrication. *Mater Sci Eng R Rep,* 144:100606.

https://doi.org/10.1016/j.mser.2021.100606

31. Al-Ketan O, Rowshan R, Abu Al-Rub RK, 2018, Topology-mechanical property relationship of 3D printed strut, skeletal, and sheet based periodic metallic cellular materials. *Addit Manuf*, 19:167–183.

https://doi.org/10.1016/j.addma.2017.12.006

32. Yánez A, Cuadrado A, Martel O, *et al.*, 2018, Gyroid porous titanium structures: A versatile solution to be used as scaffolds in bone defect reconstruction. *Mater Des*, 140:21–29.

https://doi.org/10.1016/j.matdes.2017.11.050

33. Jin Y, Kong H, Zhou X, *et al.*, 2020, Design and characterization of sheet-based gyroid porous structures with bioinspired functional gradients. *Materials (Basel)*, 13: 108971.

https://doi.org/10.3390/ma13173844

34. Yuan L, Ding S, Wen C, 2019, Additive manufacturing technology for porous metal implant applications and triple minimal surface structures: A review. *Bioact Mater*, 4:56–70.

https://doi.org/10.1016/j.bioactmat.2018.12.003

35. Soro N, Saintier N, Merzeau J, *et al.*, 2021, Quasi-static and fatigue properties of graded Ti–6Al–4V lattices produced by laser powder bed fusion (LPBF). *Addit Manuf*, 37:101653.

https://doi.org/10.1016/j.addma.2020.101653

36. Yang L, Yan C, Han C, *et al.*, 2018, Mechanical response of a triply periodic minimal surface cellular structures manufactured by selective laser melting. *Int J Mech Sci*, 148:149–157.

https://doi.org/10.1016/j.ijmecsci.2018.08.039

37. Shi J, Zhu L, Li L, *et al.*, 2018, A TPMS-based method for modeling porous scaffolds for bionic bone tissue engineering. *Sci Rep*, 8:7395.

https://doi.org/10.1038/s41598-018-25750-9

38. Zadpoor AA, 2019, Mechanical performance of additively manufactured meta-biomaterials. *Acta Biomater*, 85:41–59.

https://doi.org/10.1016/j.actbio.2018.12.038

39. Kapfer SC, Hyde ST, Mecke K, *et al.*, 2011, Minimal surface scaffold designs for tissue engineering. *Biomaterials*, 32:6875–6882.

https://doi.org/10.1016/J.BIOMATERIALS.2011.06.012

40. Zhao S, Li SJ, Wang SG, *et al.*, 2018, Compressive and fatigue behavior of functionally graded Ti-6Al-4V meshes fabricated by electron beam melting. *Acta Mater*, 150:1–15.

https://doi.org/10.1016/j.actamat.2018.02.060

41. Dong Z, Zhao X, 2021, Application of TPMS structure in bone regeneration. *Eng Regen*, 2:154–162.

https://doi.org/10.1016/J.ENGREG.2021.09.004

42. Liu F, Ran Q, Zhao M, *et al.*, 2020, Additively manufactured continuous cell-size gradient porous scaffolds: Pore characteristics, mechanical properties and biological responses in vitro. *Materials (Basel, Switzerland)*, 13:2589.

https://doi.org/10.3390/MA13112589

43. Yadroitsava I, du Plessis A, Yadroitsev I, 2019, Bone regeneration on implants of titanium alloys produced by laser powder bed fusion: A review, in *Titanium for Consumer Applications: Real World Use of Titanium*, 197–233.

https://doi.org/10.1016/B978-0-12-815820-3.00016-2

44. Bobyn JD, Pilliar RM, Cameron HU, *et al.*, 1980, The optimum pore size for the fixation of porous surfaced metal implants by the ingrowth of bone. *Clin Orthop Relat Res*, 150:263–270.

https://doi.org/10.1097/00003086-198007000-00045

45. Wang Z, Zhang M, Liu Z, *et al.*, 2022, Biomimetic design strategy of complex porous structure based on 3D printing Ti-6Al-4V scaffolds for enhanced osseointegration. *Mater Des*, 218:110721.

https://doi.org/10.1016/j.matdes.2022.110721

46. Taniguchi N, Fujibayashi S, Takemoto M, *et al.*, 2016, Effect of pore size on bone ingrowth into porous titanium implants fabricated by additive manufacturing: An in vivo experiment. *Mater Sci Eng C*, 59:690–701.

https://doi.org/10.1016/j.msec.2015.10.069

47. Mahmoud D, Elbestawi MA, 2019, Selective laser melting of porosity graded lattice structures for bone implants. *Int J Adv Manuf Technol*, 100:2915–2927.

https://doi.org/10.1007/s00170-018-2886-9

48. Surmeneva MA, Surmenev RA, Chudinova EA, *et al.*, 2017, Fabrication of multiple-layered gradient cellular metal scaffold via electron beam melting for segmental bone reconstruction. *Mater Des*, 133:195–204.

https://doi.org/10.1016/j.matdes.2017.07.059

49. Tüzemen MÇ, Salamcı E, Ünal R, 2022, Additive manufacturing design approach to strut-based functionally graded porous structures for personalized implants. *J Manuf Process*, 84:1526–1540.

https://doi.org/10.1016/J.JMAPRO.2022.10.045

50. Tüzemen MÇ, Salamcı E, Ünal R, 2022, Investigation of the relationship between flexural modulus of elasticity and functionally graded porous structures manufactured by AM. *Mater Today Commun*, 31:103592.

https://doi.org/10.1016/J.MTCOMM.2022.103592

51. Murat Dursun A, Çağrı Tüzemen M, Salamci E, *et al.*, 2022, Investigation of compatibility between design and additively manufactured parts of functionally graded porous structures. *J Polytech*, 25:1069–1082.

https://doi.org/10.2339/POLITEKNIK.891080

52. Kelly CN, Wang T, Crowley J, *et al.*, 2021, High-strength, porous additively manufactured implants with optimized mechanical osseointegration. *Biomaterials*, 279:121206.

https://doi.org/10.1016/J.BIOMATERIALS.2021.121206

53. Yang L, Wu S, Yan C, *et al.*, 2021, Fatigue properties of Ti-6Al-4V Gyroid graded lattice structures fabricated by laser powder bed fusion with lateral loading. *Addit Manuf*, 46:102214.

https://doi.org/10.1016/J.ADDMA.2021.102214

54. Kelly CN, Wang T, Crowley J, *et al.*, 2021, High-strength, porous additively manufactured implants with optimized mechanical osseointegration. *Biomaterials*, 279:121206.

https://doi.org/10.1016/j.biomaterials.2021.121206

55. Zhang J, Chen X, Sun Y, *et al.*, 2022, Design of a biomimetic graded TPMS scaffold with quantitatively adjustable pore size. *Mater Des*, 218:110665.

https://doi.org/10.1016/J.MATDES.2022.110665

56. de Galarreta SR, Doyle RJ, Jeffers J, *et al.*, 2021, Laser powder bed fusion of porous graded structures: A comparison between computational and experimental analysis. *J Mech Behav Biomed Mater*, 123:104784.

https://doi.org/10.1016/J.JMBBM.2021.104784

57. Hildebrand T, Rüegsegger P, 1997, A new method for the model-independent assessment of thickness in three-dimensional images. *J Microsc*, 185:67–75.

https://doi.org/10.1046/J.1365-2818.1997.1340694.X

58. Kolken HMA, Garcia AF, Du Plessis A, *et al.*, 2021, Fatigue performance of auxetic meta-biomaterials. *Acta Biomater*, 126:511–523.

https://doi.org/10.1016/j.actbio.2021.03.015

59. ASTM-E407 | Standard Practice for Microetching Metals and Alloys | Document Center, Inc.

60. ISO - ISO 13314:2011 - Mechanical testing of metals—Ductility testing—Compression test for porous and cellular metals.

61. Benedetti M, Klarin J, Johansson F, *et al.*, 2019, Study of the compression behaviour of Ti6Al4V trabecular structures produced by additive laser manufacturing. *Materials (Basel)*, 12:1471.

https://doi.org/10.3390/MA12091471

62. Benedetti M, Galeotti F, Emanuelli L, *et al.*, 2019, Deformation behaviour of Ti-6Al-4V trabecular structures produced by additive laser manufacturing. *Euro PM 2019 Congr Exhib.*

63. Schmitz A, Horst P, 2014, A finite element unit-cell method for homogenised mechanical properties of heterogeneous plates. *Compos Part A Appl Sci Manuf*, 61:23–32.

https://doi.org/10.1016/J.COMPOSITESA.2014.01.014

64. Alwattar TA, Mian A, 2019, Development of an elastic material model for BCC lattice cell structures using finite element analysis and neural networks approaches. *J Compos Sci*, 3:33.

https://doi.org/10.3390/JCS3020033

65. Kim HS, Al-Hassani STS, 2003, Effective elastic constants of two-dimensional cellular materials with deep and thick cell walls. *Int J Mech Sci*, 45:1999–2016.

https://doi.org/10.1016/J.IJMECSCI.2004.02.002

66. Webb DC, Kormi K, Al-Hassani STS, 1995, Use of FEM in performance assessment of perforated plates subject to general loading conditions. *Int J Press Vessel Pip*, 64: 137–152.

https://doi.org/10.1016/0308-0161(94)00078-W

67. Murchio S, Dallago M, Zanini F, *et al.*, 2021, Additively manufactured Ti–6Al–4V thin struts via laser powder bed fusion: Effect of building orientation on geometrical accuracy and mechanical properties. *J Mech Behav Biomed Mater*, 119:104495.

https://doi.org/10.1016/J.JMBBM.2021.104495

68. Gordon JV, Narra SP, Cunningham RW, *et al.*, 2020, Defect structure process maps for laser powder bed fusion additive manufacturing. *Addit Manuf*, 36:101552.

https://doi.org/10.1016/J.ADDMA.2020.101552

69. Abdulhadi HS, Mian A, 2019, Effect of strut length and orientation on elastic mechanical response of modified body-centered cubic lattice structures. *Proc Inst Mech Eng Part L: J Mater Des Appl*, 233:2219–2233.

https://doi.org/10.1177/1464420719841084

70. Alkhatib SE, Tarlochan F, Mehboob H, *et al.*, 2019, Finite element study of functionally graded porous femoral stems incorporating body-centered cubic structure. *Artif Organs*, 43:E152–E164.

https://doi.org/10.1111/AOR.13444

71. Yang L, Li Y, Wu S, *et al.*, 2022, Tailorable and predictable mechanical responses of additive manufactured TPMS lattices with graded structures. *Mater Sci Eng A*, 843:143109.

https://doi.org/10.1016/J.MSEA.2022.143109

72. Lv Y, Wang B, Liu G, *et al.*, 2022, Design of bone-like continuous gradient porous scaffold based on triply periodic minimal surfaces. *J Mater Res Technol*, 21:3650–3665.

https://doi.org/10.1016/J.JMRT.2022.10.160

73. Belda R, Megías R, Marco M, *et al.*, 2023, Numerical analysis of the influence of triply periodic minimal surface structures morphometry on the mechanical response. *Comput Methods Programs Biomed*, 230:107342.

https://doi.org/10.1016/J.CMPB.2023.107342